

# MID-INFRARED DIAGNOSTICS OF STARBURST GALAXIES: CLUMPY, DENSE STRUCTURES IN STAR-FORMING REGIONS IN THE ANTENNAE (NGC 4038/4039)<sup>1</sup>

LEONIE SNIJDERS<sup>2</sup>, LISA J. KEWLEY<sup>3</sup> & PAUL P. VAN DER WERF<sup>2</sup>

*Draft version November 5, 2018*

## ABSTRACT

Recently, mid-infrared instruments have become available on several large ground-based telescopes, resulting in data sets with unprecedented spatial resolution at these long wavelengths. In this paper we examine 'ground-based-only' diagnostics, which can be used in the study of star-forming regions in starburst galaxies. By combining output from the stellar population synthesis code *Starburst 99* with the photoionization code *Mappings*, we model stellar clusters and their surrounding interstellar medium, focusing on the evolution of emission lines in the N- and Q-band atmospheric windows (8 – 13 and 16.5 – 24.5  $\mu\text{m}$  respectively) and those in the near-infrared. We address the detailed sensitivity of various emission line diagnostics to stellar population age, metallicity, nebular density, and ionization parameter. Using our model results, we analyze observations of two stellar clusters in the overlap region of the Antennae galaxies obtained with VLT Imager and Spectrometer for mid Infrared (VISIR). We find evidence for clumpy, high density, ionized gas. The two clusters are young (younger than 2.5 and 3 Myr respectively), the surrounding interstellar matter is dense ( $\geq 10^4 \text{ cm}^{-3}$ ) and can be characterized by a high ionization parameter ( $\log U \geq -1.53$ ). Detailed analysis of the mid-infrared spectral features shows that a (near-)homogeneous medium cannot account for the observations, and that complex structure on scales below the resolution limit, containing several young stellar clusters embedded in clumpy gas, is more likely.

*Subject headings:* galaxies: individual (NGC4038/4039) — galaxies: starburst, star clusters — ISM: HII regions — infrared: ISM

## 1. INTRODUCTION

With a star formation rate (SFR) of several tens to several hundreds of solar masses a year, starburst galaxies form stars at a much higher rate than regular gas-rich galaxies. As a result, starburst galaxies empty their gas reservoirs quickly during a short, vigorous burst of star-formation. This short-lived starburst phase is generally initiated by interactions with neighbor galaxies, causing distortions in the galaxy's gravitational potential. As a consequence molecular gas piles up, and in the resulting concentrations of very dense gas active star formation takes place. Although locally rare, because of the limited duration of the starburst phase and the relatively low galaxy pair density in the local universe, starburst galaxies are a very important piece in the puzzle of galaxy evolution. In a very short time the galaxy's morphology and stellar content are significantly altered, and the interstellar and even intergalactic medium is rapidly enriched. At higher redshifts starburst galaxies are a much more common phenomenon, and sub-mm observations indicate that the intense outbursts of star formation in these objects might be the dominant mode of star formation in the high- $z$  universe (e.g. Heckman 1998; Blain et al. 1999; Smail et al. 2002, and many others). Despite numerous studies of starburst galaxies, several issues remain unsolved, like the exact mechanism that ignites and shuts off the starburst phase, and the mass

function of the individual stellar populations formed during the bursts.

In this work we focus on the individual star-forming regions formed during these starbursts. With a wealth of young, bright stellar clusters, starburst galaxies are excellent objects for the study of the physical processes of star formation. This is why starburst galaxies play an important role in the debate on the universality of the stellar Initial Mass Function (IMF, Kroupa 2007). Since star formation takes place in dusty giant molecular clouds, the active star-forming regions in starburst galaxies generally suffer from high obscuration. This makes the (mid-)infrared a favorable regime for the study of the youngest, most massive, deeply embedded stellar populations. Analysis of mid-infrared nebular emission lines of clusters in starburst galaxies have led to various different conclusions on the IMF of these objects. Contrary to what one would expect for young, massive stellar populations, ISO measured relatively low values for the  $[\text{Ne III}]/[\text{Ne II}]$  ratio, indicating a soft UV radiation field. Thornley et al. (2000) suggest that the soft radiation field is a result from the aging of stellar populations with a 'regular' IMF (up to  $M_{\text{up}} \sim 50 - 100 M_{\odot}$ ), formed in short-lived bursts of star formation (1 – 10 Myr). Alternative explanations are a truncated IMF, lacking massive stars, or massive stars spending a considerable fraction of their lifetime embedded in an ultra compact (UC)H II region, hidden from view even at mid-infrared wavelengths (Rigby & Rieke 2004). In relation to this discussion, Martín-Hernández et al. (2002) already pointed out the need for a more comprehensive study of mid-infrared diagnostics, since the neon ratio is not only sensitive to radiation hardness, but to metallic-

<sup>1</sup> Based on observations collected at the European Southern Observatory, Paranal, Chile, under program no. 075.B-0727(A), 075.B-0791(A), and 69.B-0688(A)

<sup>2</sup> Leiden Observatory, Leiden University, PO Box 9513, 2300 RA Leiden, The Netherlands

<sup>3</sup> University of Hawaii, 2680 Woodlawn Drive, Honolulu, USA

ity, nebular density and ionization parameter as well.

Over the last decades the field of mid-infrared astronomy received an enormous impulse from observations with space telescopes; from Infrared Astronomical Satellite (IRAS) in the eighties, Infrared Space Observatory (ISO) in the nineties and currently from the Spitzer Space Telescope. However, as discussed by Martín-Hernández et al. (2005), the interpretation of large aperture mid-infrared observations obtained with space telescopes can be challenging, especially for extragalactic objects. Ground-based mid-infrared astronomy faces additional challenges due to the characteristics of the earth's atmosphere, but thanks to rapid progress in detector technology, several mid-infrared instruments have become available on large ground-based observatories in the past five years. Compared to observations from space, ground-based work offers the considerable advantage of a more detailed view of the objects of interest, due to the much higher spatial resolution that can be obtained. For example, the typical size of a star-forming region is a few to a few tens of parsecs. With its 85 cm mirror, Spitzer can resolve details on a 50 parsec scale in objects out to 4 Mpc distance. With an 8 meter class telescope similar scales can be resolved out to 40 Mpc, increasing the volume that can be probed at this resolution by a factor of a thousand. Unfortunately, the atmosphere is opaque to most infrared radiation, making it impossible to access the full infrared wavelength regime from the ground. This means that we are limited to a number of specific atmospheric windows of (reasonably) good transmission; the L band between 3.0 and 4.0  $\mu\text{m}$ , the M band in the range of 4.6 to 5.2  $\mu\text{m}$ , the N band from 8 to 13  $\mu\text{m}$  and the Q band between 16.5 and 24.5  $\mu\text{m}$ . The aim of this paper is to explore the spectral diagnostic features available for the study of star-forming regions within these windows, combining near- and mid-infrared wavelengths (J, H, K, L, N and Q band, roughly covering 1 – 25  $\mu\text{m}$ ). We will address the behavior of near- and mid-infrared emission line ratios as a function of cluster age, gas pressure, metallicity, and ionization parameter.

In Section 2 we discuss the spectral features observable with ground-based facilities and the codes used in our model efforts, the stellar population synthesis model, *Starburst 99*, and the photoionization code *Mappings*, as well as the model grid input parameters. The model results are presented in Section 3, and compared with existing models in Section 4. In Section 5 diagnostic diagrams are introduced, which are compared to mid-infrared data of H II regions from the literature in Section 6. In Section 7 we present mid-infrared spectroscopic observations of clusters in the Antennae overlap regions. In Section 8 these data are analyzed and our results are discussed. Finally, we summarize our findings in Section 9.

## 2. MODELING THE EMISSION LINE SPECTRA

Our work focuses on stellar populations created during vigorous bursts of star formation in starburst galaxies. These stellar populations are young, dust-enshrouded star clusters, still embedded in their natal clouds. To model these systems we combine the stellar population synthesis model, *Starburst 99* (Leitherer et al. 1999), with the photoionization code *Mappings IIIr* (Dopita et al. 2000, 2002; Groves, Dopita & Sutherland

2004). We constructed a grid covering a large parameter space, exploring a range of metallicities, ISM densities and ionization parameters for clusters of ages ranging from 0 to 6 Myr.

### 2.1. Spectral features in the wavelength range of the atmospheric windows

In the near- and mid-infrared wavelength range a wealth of spectral features is available to probe the characteristics of the emitting source, in our case embedded stellar clusters. For these systems, the near-infrared bands are dominated by bright hydrogen and helium recombination lines. When the clusters reach the age at which the red super giant stars appear, these start dominating the near-infrared continuum and, in the K band, CO absorption bands appear. The spectral region around 10  $\mu\text{m}$  (the N band) displays a complex combination of silicate absorption, fine-structure emission lines originating from various species and emission by Polycyclic Aromatic Hydrocarbon (PAH) molecules. Longwards of the N band, the mid-infrared is dominated by thermal continuum emission of dust, with fine-structure lines and PAH emission bands (though much less prominent than in the N band) superposed on it. Furthermore, in both the near- and mid-infrared strong molecular hydrogen  $\text{H}_2$  lines can be found. In this paper we focus exclusively on the emission lines.

With ground-based observations, information between the atmospheric windows is unobservable, for instance the [Ne III] line at 15.56  $\mu\text{m}$  between the N and Q band window. For this reason it is impossible to use [Ne III]/[Ne II] ratio, which is a good diagnostic for the hardness of the radiation field. Longwards of the Q band window there are several other fine-structure lines unobservable with ground-based facilities. Most of them are not straightforward to interpret: both the [O IV] and the [Fe II] line around 26  $\mu\text{m}$  can be strongly affected by shocks. The [Si II] line at 34.82  $\mu\text{m}$  is also very complex to analyse, since it is not only excited in H II regions, but in Photon Dominated Regions (PDR) and X-ray Dominated Regions (XDR) as well. The only line with a relatively simple excitation mechanism at these longer wavelengths accessible to Spitzer is the [S III] line at 33.48  $\mu\text{m}$ . Combined with the [S III] line at 18.71  $\mu\text{m}$  this emission line forms a very useful density diagnostic, which is unfortunately not available in ground-based observations.

We will address some of the emission lines only accessible with space-based telescopes, like the [Ne III] 15.56  $\mu\text{m}$  and the [S III] 33.48  $\mu\text{m}$  lines, in order to test our model results with mid-infrared databases of starburst galaxies (obtained with ISO and Spitzer, large databases observed with ground-based mid-infrared facilities are not yet available in the literature). However, the main focus of this paper is the modeling of ground-based near- and mid-infrared observations. The lines we have available in these observations are the series of bright hydrogen and helium recombination lines in the near-infrared bands plus several fine-structure lines in the mid-infrared: [Ar III] at 8.99  $\mu\text{m}$ , [S IV] at 10.51  $\mu\text{m}$  and [Ne II] at 12.81  $\mu\text{m}$  in the N band and [S III] at 18.71  $\mu\text{m}$  in the Q band.

### 2.2. Stellar population synthesis model

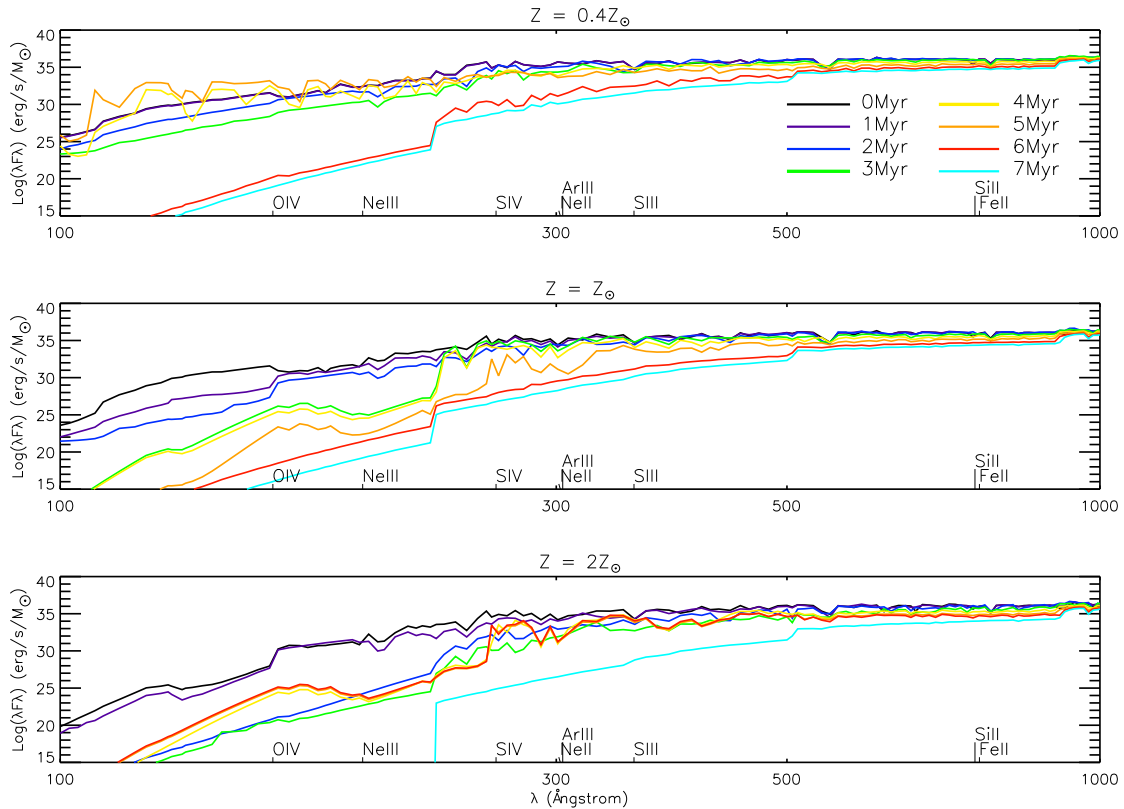


FIG. 1.— FUV spectra as computed by *Starburst 99* as a function of starburst age for *upper*:  $0.4Z_{\odot}$ , *middle*:  $1Z_{\odot}$  and *lower*:  $2Z_{\odot}$ . Ionization thresholds for a number of relevant elements are shown.

We use the recently released version (5.1) of *Starburst 99* to model the spectral energy distributions (SEDs) of stellar clusters. The code constructs these SEDs by summing the luminosity-weighted spectra of the individual stars according to the chosen IMF, following theoretical stellar evolutionary tracks for each star from Zero Age Main Sequence (ZAMS) to its final stage. As we only study the youngest phases of star formation, the ionizing spectrum is dominated by O and B stars. The Geneva evolutionary tracks, which are optimized for modeling high-mass stars, are used to calculate the SEDs, applying the high mass loss rate models as recommended by Maeder & Meynet (1994). Kurucz’s stellar atmosphere models as compiled by Lejeune (Kurucz et al. 1992; Lejeune et al. 1997) are applied for stars without strong winds, for which the static, plane-parallel atmospheres are a good approximation. For stars with strong winds Smith et al. (2002) implemented non-LTE, line-blanketed model atmospheres for Wolf-Rayet (W-R, Hillier & Miller 1998) and O stars (Pauldrach et al. 2001). The switch between extended and plane-parallel atmospheres is as described in Leitherer & Heckman (1995). A detailed description of the changes of version 5.0 compared to 4.0 can be found in Vázquez & Leitherer (2005). Version 5.1 is similar to 5.0, with updates in the density and supernova routines<sup>1</sup>.

We created three sets of models to cover a range in metallicities,  $0.4Z_{\odot}$ ,  $1Z_{\odot}$  and  $2Z_{\odot}$  ( $Z=0.008$ ,  $Z=0.02$  and  $Z=0.04$ ; the solar abundance set is listed in Table 1). For

each of these metallicities we modeled an instantaneous burst of star formation, in which a million solar masses of stars are formed following a Salpeter IMF between 0.1 and  $100 M_{\odot}$ . To ensure that the chosen cluster mass of  $10^6 M_{\odot}$  does not induce an artificial upper mass cutoff, the spectral type distribution of the resulting stellar populations was examined. At 0 Myr the highest mass bin (O3 star) contains several stars, confirming that the populations fully sample all spectral types up to  $100 M_{\odot}$ . The spectra are calculated in 1 Myr time steps between 0 and 6 Myr and additionally at 2.5 and 3.5 Myr. For the  $2Z_{\odot}$  models the spectra are calculated at 7 Myr as well, because of the extended lifetime of the W-R phase at high metallicity (see Section 3.1).

Figure 1 shows the *Starburst 99* ionizing spectra (far-ultraviolet (FUV) between 100 and 1000 Å) as a function of age and metallicity. The hardness of the radiation decreases with age, because the highest mass stars evolve off the main sequence. This effect is seen most clearly at the shortest wavelengths, between 100 – 300 Å. Longwards of 300 Å the SEDs are very similar for all metallicities, particularly during the first four million years. At the highest energies (between 100 and 300 Å) the sub-solar metallicity spectrum is significantly harder than the super-solar one. This difference increases with age. Higher metallicity stars spend a larger fraction of their high energy photons ionizing the metals in their own atmospheres (line-blanketing). Therefore, fewer photons are available to ionize the surrounding matter, giving a softer SED. Furthermore, low metallicity stars of similar spectral type have a higher effective temperature than

<sup>1</sup> This information comes from the *Starburst 99* website: <http://www.stsci.edu/science/starburst99/>.

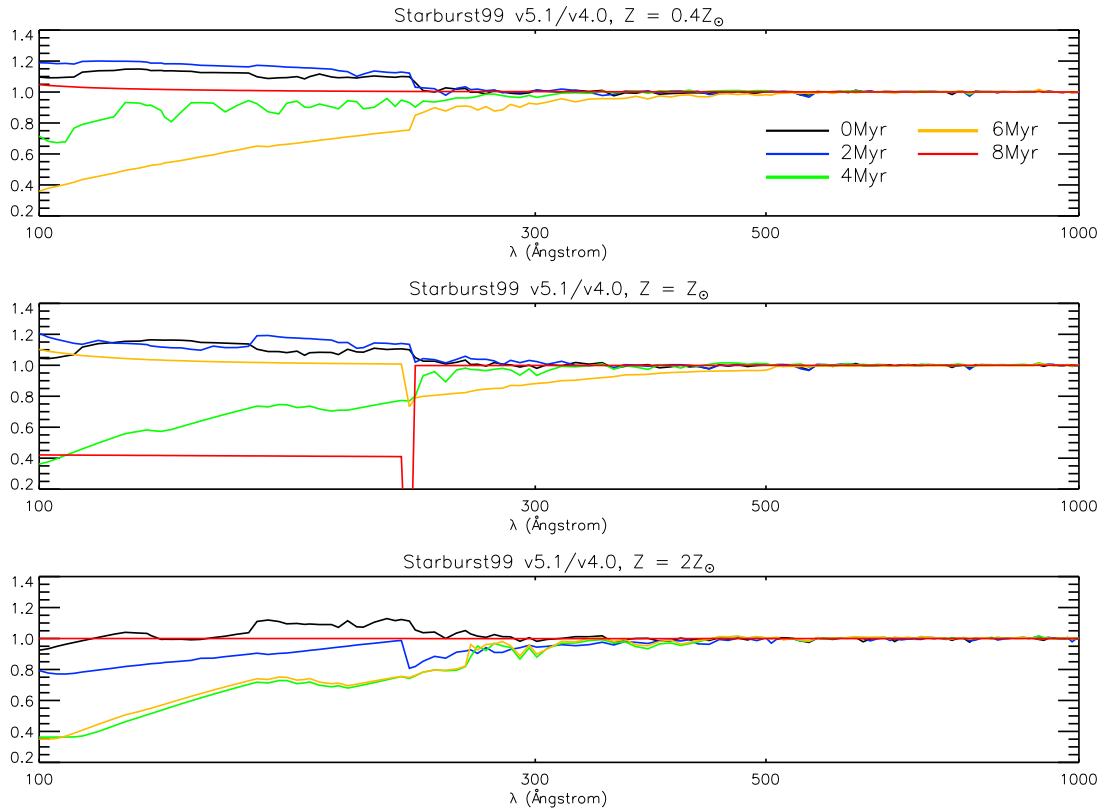


FIG. 2.— Comparison of the FUV spectra computed with the new *5.1 Starburst 99* version and the original *4.0* version. The curves show the *v5.1* spectrum divided by the *v4.0* spectrum for various ages for *upper*:  $0.4Z_{\odot}$ , *middle*:  $1Z_{\odot}$  and *lower*:  $2Z_{\odot}$ .

high metallicity stars, also contributing to a harder spectrum at low metallicity. Around 3 Myr the first massive stars enter the W-R phase, causing temporary hardening of the SED. This manifests itself as a bump around the [O IV] ionization threshold between 3 and 5 Myr in the  $Z_{\odot}$  spectra (between 3 and 6 Myr for  $2Z_{\odot}$ ). In the  $0.4Z_{\odot}$  spectra the SED shows a larger number of high energy photons over the whole 100 – 300 Å range in the W-R phase, making the spectra between 4 and 5 Myr harder than at 0 Myr. The sharp edge at 228 Å in the spectra at 6/7 Myr corresponds to the He II ionization edge (54.42 eV). At these ages there are few photons available for the excitation of species with an excitation potential exceeding that of He II (like [Ne III] and [O IV]).

The FUV spectra have changed significantly since the *Starburst 99 4.0* version. Figure 2 shows the effect of the implementation of sophisticated atmospheric models, including metal line-blanketing and non-LTE O-star atmospheres (*v4.0* only treated radiative transfer for hydrogen and helium and assumed LTE for stars of all masses). The plots show the new *Starburst 99 v5.1* spectra divided by the output of the old version of the code (*v5.1/v4.0*). The largest differences occur shortwards of 300 Å. At the youngest ages (0 – 2 Myr for  $0.4Z_{\odot}$  and  $Z_{\odot}$  and at 0 Myr for  $2Z_{\odot}$ ) the new version produces 5 – 20% more He II ionizing photons ( $< 300 \text{ \AA}$ ) than *v4.0*. Between 2 – 6 Myr, the FUV spectra ( $< 300 \text{ \AA}$ ) of the old version harden where the output spectra of the new version show a gradual softening with age, as discussed above. The relative amount of high energy photons available in the *v5.1* spectra between 2 – 6 Myr can be as much as

20% (at 250 Å) to 60% (at 100 Å) lower compared to the old version. This shows that a considerable fraction of photons at these energies is used to ionize the stellar atmospheres. Around 6 or 7 Myr (depending on metallicity) the old and new version give roughly identical output spectra. To conclude, characteristics of young stellar populations and/or their surroundings derived from emission lines sensitive to emission in this wavelength range alter significantly with these recent improvements of the code.

### 2.3. Photoionization model

The *Starburst 99* output spectra are fed into the photoionization code *Mappings* to model the combined SED of a stellar cluster plus the irradiated surrounding gaseous medium. The code combines photoionization theory with radiation pressure and the effects of dust. The cloud’s ionization structure is determined by the ionization parameter  $q$  at the inner cloud boundary:

$$q = \frac{Q_{\text{Lyc}}}{4\pi R^2 n_{\text{ion}}} \quad (1)$$

$Q_{\text{Lyc}}$  being the hydrogen ionizing photon flux,  $R$  the radius of the inner cloud boundary, and  $n_{\text{ion}}$  the ion density (which equals  $\approx 1.1$  times the hydrogen density  $n_H$  if we account for helium ionization). The ionization parameter  $q$  measures the density of ionizing photons relative to the atomic density. It relates to the commonly used dimensionless ionization parameter  $U$  through  $U \equiv 1.1 \cdot q/c$ . We assume that the object’s radius  $R$  is much larger than the thickness of the emitting shell of

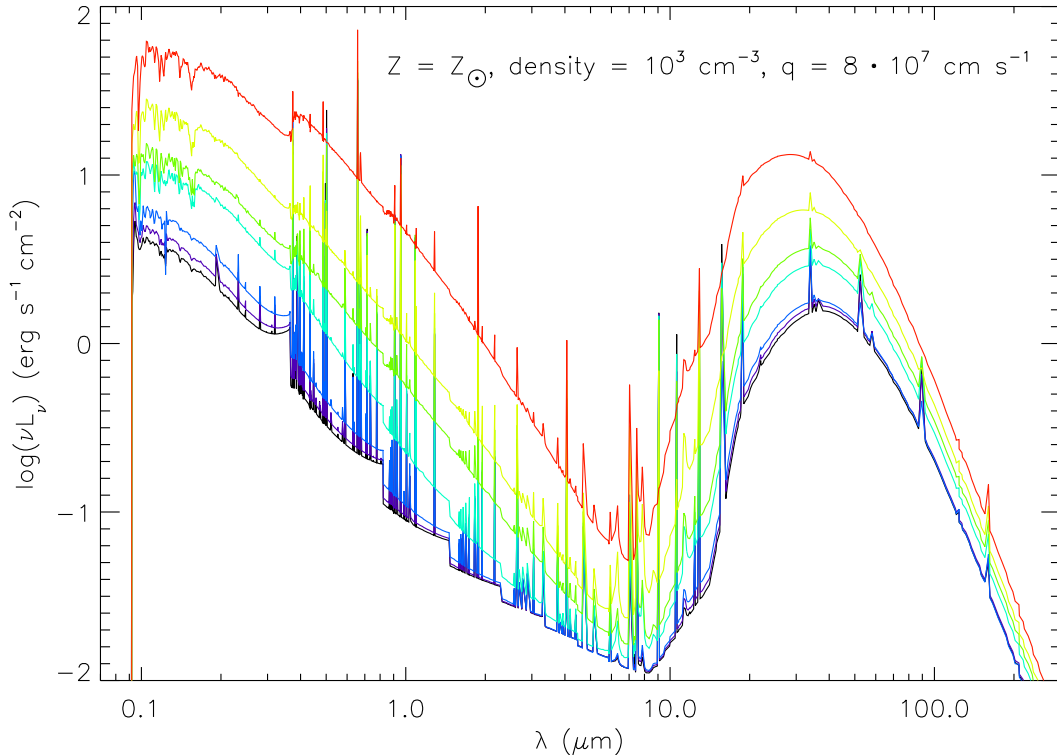


FIG. 3.— Example of *Mappings* output spectra. Solar metallicity model with a density of  $10^3 \text{ cm}^{-3}$  and an ionization parameter  $q$  of  $8 \cdot 10^7 \text{ cm s}^{-1}$ . The age increases from *lowest*: 0 Myr to *upper*: 6 Myr, in steps of 1 Myr (color version available in electronic edition). Note the nebular bound-free edges, the strong recombination and fine-structure emission lines and the far-infrared peak originating from heated dust.

TABLE 1  
SOLAR ABUNDANCE & METALLICITY SCALING

Element	Abundance <sup>a</sup>	Depletion <sup>b</sup>
H .....	0.000	0.00
He.....	-1.01	0.00
C .....	-3.59	-0.30
N .....	-4.20	-0.22
O .....	-3.34	-0.07
Ne.....	-3.91	0.00
Na.....	-5.75	-1.00
Mg.....	-4.42	-0.70
Al.....	-5.61	-1.70
Si.....	-4.49	-1.00
S .....	-4.79	0.00
Cl.....	-6.40	-1.00
Ar.....	-5.20	0.00
Ca.....	-5.64	-2.52
Fe.....	-4.55	-2.00
Ni.....	-5.68	-2.00

<sup>a</sup> All abundances are logarithmic with respect to Hydrogen

<sup>b</sup> Depletion given as  $\log(X/H)_{\text{gas}} - \log(X/H)_{\text{ISM}}$

gas. In this case a plane-parallel geometry is a good approximation, which we applied in our models. As the code steps through the interstellar cloud, *Mappings* calculates the energy balance for each thin slab by coupling detailed modeling of the atomic gas processes with the dust physics. Photoionization, collisional ionization and recombination processes are taken into account, as well as photoelectric heating of the gas by the dust, radia-

tion pressure acting on the dust and charge transfer reactions. In this way the (FUV) photons from the input spectrum are reprocessed by the ISM surrounding the star cluster. For each given combination of input SED, metallicity, density and ionization parameter the photoionization code gives a unique emission line spectrum (see Fig. 3 and a detailed description in Section 3).

The dust is modeled by a combination of two types of grains, amorphous silicates and amorphous carbon grains. Together these adequately reproduce both continuum emission in the infrared and extinction at shorter wavelengths (Draine 2003; Dopita et al. 2005). The grain sizes follow a power law distribution with a slope consistent with the grain shattering model (Jones et al. 1996),  $\alpha = -3.3$ , modified to allow for a lower and upper size cutoff of 40 Å and 1600 Å respectively (see Equation 19 in Dopita et al. 2005). *Mappings* divides the grains into 80 size bins and computes the absorption, scattering, and photoelectric heating for each bin (in older versions of the code photoelectric heating was calculated for the dust as a whole). The results are then used to calculate the dust temperature, which determines the mid- and far-infrared continuum emission. While only two simple types of dust are considered in the calculation of dust extinction and emission, all elements with a high enough gas phase condensation temperature ( $> \text{few } 100 \text{ K}$ ) are depleted. Depletion factors are assumed to be identical to those in the local ISM (Savage & Sembach 1996). The depletion set is listed in Table 1.

Although PAH features have been observed routinely

ever since their discovery two decades ago, exact knowledge on PAH shapes, size distributions and their interplay with the environment still remains too poor for PAHs to be modeled adequately. In *Mappings* PAHs are represented by a single type, coronene ( $C_{24}H_{12}$ ), for which the abundance is determined by the amount of carbon depleted onto PAH molecules (fraction here chosen to be 0.05). For this one specific PAH molecule absorption, emission, and photoelectric processes are calculated in detail to represent the PAH infrared spectrum (Dopita et al. 2005, and references therein).

#### 2.4. Parameter space covered by the model grid

The model input parameters for *Mappings* were chosen to mimic the wide spectrum of observed nebular conditions in H II regions, covering low-density to UCH II regions. For a range in ages (0 – 6/7 Myr) and metallicities ( $0.4Z_{\odot}$ ,  $Z_{\odot}$  and  $2Z_{\odot}$ ) we computed plane-parallel, isobaric, dusty models with gas densities increasing from  $10^2$  to  $10^6$   $cm^{-3}$ . Likewise an appropriate range in values for the ionization parameter  $q$  (see Eq. 1) was chosen. Typical values for the ionization parameter in local starburst galaxies span  $-3 \leq \log U \leq -1.5$  (Fig. 10 in Rigby & Rieke 2004, who adopt a value for  $\log U$  of  $-2.3$  in their models). Therefore the *Starburst 99* spectra are scaled to obtain a fixed ionization parameter  $q$  at the inner cloud boundary at a value of  $2 \cdot 10^7$ ,  $4 \cdot 10^7$ ,  $8 \cdot 10^7$ ,  $1.6 \cdot 10^8$ ,  $4 \cdot 10^8$  and  $8 \cdot 10^8$   $cm s^{-1}$  (corresponding to  $\log U \approx -3.13$ ,  $-2.83$ ,  $-2.53$ ,  $-2.23$ ,  $-1.83$  and  $-1.53$ ). Scaling the *Starburst 99* spectra essentially means scaling the cluster mass. We will not address the cluster masses in present work, but we will use the mass information in future work on near-IR spectra of the same objects (Snijders & Van der Werf, in preparation).

### 3. MODEL RESULTS

Fig. 3 shows an example of the *Mappings* output spectra. The UV part of the spectrum originates from massive stars at all times. The visible and near-infrared are dominated by nebular emission up to 4 Myr, showing clear bound-free edges. Beyond 4 Myr red super giants take over the near-infrared continuum. Additionally, prominent hydrogen and helium recombination lines are found in the visible and near-infrared. The mid- and far-infrared continuum originates from heated dust, showing the characteristic far-infrared peak. In the mid-infrared N band around  $10 \mu m$  the SED is dominated by a combination of fine-structure lines, silicate absorption and PAH features.

The peak of the hot dust continuum is seen to shift towards shorter wavelengths, indicating higher dust temperatures, with increasing age (and thus softer ionizing spectrum). This is caused by the way we define the *Mappings* input parameters. The *Starburst 99* input spectra, pressure and temperature are scaled to keep the density and ionization parameter at certain fixed values. A softer input spectrum requires a larger scaling factor to obtain the same amount of ionizing photons. This results automatically in a larger number of photons in the soft-UV and visible regime with increasing age. These photons do not affect the mid-infrared fine-structure lines, since these lines are exclusively excited by high energy UV photons. The dust however is heated by both. Altogether, for a fixed value of the ionization parameter, there are

more photons available at higher age to heat the dust, causing the far-infrared peak to shift to shorter wavelengths.

#### 3.1. Age evolution of line ratios: mid-infrared

Ratios of lines with different excitation potentials can be used to measure the temperature of the radiation field. Unfortunately the interpretation of these line ratios is complicated by the fact that they are sensitive to metallicity of the ionizing cluster, ISM density and ionization parameter as well. This effect is demonstrated in Figures 4 and 5, in which the evolution of various emission line ratios with cluster age is shown. Line ratios involving emission lines that have (almost) identical excitation potentials, but different critical densities, are useful as density probes.

To be able to compare our model results with models from the literature we discuss the temperature-sensitive ratios  $[Ne III]_{15.56\mu m}/[Ne II]_{12.81\mu m}$  and  $[S IV]_{10.51\mu m}/[S III]_{18.71\mu m}$  and the density-sensitive ratio  $[S III]_{33.48\mu m}/[S III]_{18.71\mu m}$ , even though some of these ratios involve lines observable from space only. If we focus on the emission lines that are observable from the ground, we are limited to  $[Ar III]_{8.99\mu m}$ ,  $[S IV]_{10.51\mu m}$  and  $[Ne II]_{12.81\mu m}$  in the N band and  $[S III]_{18.71\mu m}$  in the Q band. So, in addition we examine the ‘ground-based’ line ratios temperature-sensitive ratio  $[S IV]_{10.51\mu m}/[Ar III]_{8.99\mu m}$  and the density-sensitive ratio  $[S III]_{18.71\mu m}/[Ne II]_{12.81\mu m}$ .

The line ratios are later combined to form diagnostic ratio-ratio plots (see Section 5). First,  $[S IV]/[S III]$  is plotted versus  $[Ne III]/[Ne II]$  to construct the commonly used diagnostic diagram sensitive to the hardness of the ionizing radiation. Secondly, the emission lines that are accessible from the ground are combined to form an extinction independent diagnostic diagram, plotting  $[S IV]/[Ar III]$  versus  $[S III]/[Ne II]$ . Adopting a standard Draine (1989) extinction curve, the intrinsic values of  $[S IV]/[Ar III]$  and  $[S III]/[Ne II]$  differ from the observed ratios by less than 3%, which is much less than the calibration uncertainties of our observations. These ratios are thus essentially unaffected by reddening.

Note that all mid-infrared fine-structure lines under study here are generated by  $\alpha$ -elements (neon, argon and sulphur), so abundance ratios are expected to be approximately fixed. All differences in the line ratio behavior with metallicity originate from other processes.

As the stellar population ages and massive stars evolve off the main sequence, the FUV spectrum softens causing ratios of high to low ionization lines like  $[Ne III]/[Ne II]$  to drop. The most massive star present at 2.5 Myr is an O5.5 star. At later ages the line ratios show an upturn corresponding to the appearance of W-R stars, which dominate the radiation field until the age of 6 Myr (see Figs. 4 and 5).

High metallicity stars have softer FUV spectra than low metallicity stars of similar mass due to line-blanketing within the stellar atmospheres. This explains the offset towards lower values in the  $[Ne III]/[Ne II]$  ratio with increasing metallicity as well as the steeper drop in the ratio in the first 2 – 3 Myr (see upper panel in Fig. 4). After exhaustion of hydrogen burning in the core, stellar atmosphere temperatures can drop to low enough val-

ues to initiate the W-R phase of high mass loss. Apart from having softer spectra initially, metal-rich stars can cool more efficiently, causing their W-R phase to start earlier than that of metal-poor stars. The first W-R stars appear at 2 Myr for  $2Z_{\odot}$ , 2.5 Myr for  $Z_{\odot}$  and 3 Myr for  $0.4Z_{\odot}$ . Furthermore, the phase in which W-R stars dominate the FUV spectrum lasts longer in the high metallicity case. Since metals are more abundant in their stellar atmospheres, lower mass metal-rich stars can generate enough radiation pressure to enter the W-R phase, where metal-poor stars of similar mass cannot. This effect extends the W-R phase to higher ages in the  $2Z_{\odot}$  population, which is apparent from high values for  $[\text{Ne III}]/[\text{Ne II}]$  up to 6 Myr.

Given the values of the critical densities ( $1.8 \cdot 10^5$  and  $6.1 \cdot 10^5 \text{ cm}^{-3}$  for  $[\text{Ne III}]_{15.56\mu\text{m}}$  and  $[\text{Ne II}]_{12.81\mu\text{m}}$  respectively; all values for critical densities are obtained from Tielens 2005) the  $[\text{Ne III}]/[\text{Ne II}]$  is mostly sensitive to densities between  $10^4$  and  $10^6 \text{ cm}^{-3}$ . The ratio decreases with approximately a factor of three if density increases from  $10^4$  to  $10^6 \text{ cm}^{-3}$ . Furthermore, the  $[\text{Ne III}]/[\text{Ne II}]$  ratio is sensitive to the ionization parameter, because a larger value of  $q$  means that more ionizing photons are available per atom. The  $[\text{Ne III}]/[\text{Ne II}]$  ratio increases more than an order of magnitude when  $q$  increases from  $2 \cdot 10^7$  to  $8 \cdot 10^8 \text{ cm s}^{-1}$ .

The evolution of  $[\text{S IV}]/[\text{S III}]$  shows similar behavior as  $[\text{Ne III}]/[\text{Ne II}]$ , with subtle differences due to (1) the specific sensitivity of the various individual lines to the spectral hardness of the radiation and (2) the density of the radiating medium (lower panel in Fig. 4). With critical densities of  $3.7 \cdot 10^4 \text{ cm}^{-3}$  for  $[\text{S IV}]$  and  $1.0 \cdot 10^4 \text{ cm}^{-3}$  for  $[\text{S III}]$ ,  $[\text{S IV}]/[\text{S III}]$  is sensitive to slightly lower densities than  $[\text{Ne III}]/[\text{Ne II}]$ . The density dependence is reversed, showing an increasing line ratio with increasing density. The sensitivity to  $q$  is stronger for  $[\text{S IV}]/[\text{S III}]$  than for  $[\text{Ne III}]/[\text{Ne II}]$ . As  $q$  changes from  $2 \cdot 10^7$  to  $8 \cdot 10^8 \text{ cm s}^{-1}$  the  $[\text{S IV}]/[\text{S III}]$  line ratio increases almost two orders of magnitude.

Inspecting the evolution of  $[\text{S IV}]/[\text{Ar III}]$ , one again recognizes the same shape as for  $[\text{Ne III}]/[\text{Ne II}]$  and  $[\text{S IV}]/[\text{S III}]$  (see upper panel Fig. 5).  $[\text{S IV}]/[\text{Ar III}]$  is equally sensitive to  $q$  as  $[\text{S IV}]/[\text{S III}]$  and somewhat more sensitive to density, because the difference in critical densities between  $[\text{S IV}]$  and  $[\text{Ar III}]$  is larger than between  $[\text{S IV}]$  and  $[\text{S III}]$  ( $3.7 \cdot 10^4$  and  $3.7 \cdot 10^5 \text{ cm}^{-3}$  for  $[\text{S IV}]$  and  $[\text{Ar III}]$  respectively).

Proceeding to the density-sensitive line ratios, we note that  $[\text{S III}]_{33.48\mu\text{m}}/[\text{S III}]_{18.71\mu\text{m}}$  is most commonly used in the mid-infrared as a density estimator. Having the same excitation potential, the ratio of the double-ionized sulphur lines is mainly affected by the difference in collisional de-excitation rate. With critical densities of  $1.2 \cdot 10^3$  and  $1.0 \cdot 10^4 \text{ cm}^{-3}$  for the  $[\text{S III}]_{33.48 \mu\text{m}}$  and the  $18.71 \mu\text{m}$  line respectively, the  $[\text{S III}]/[\text{S III}]$  ratio is most sensitive in the density range between  $10^2$  and  $10^4 \text{ cm}^{-3}$ , as can be seen in Fig. 6. Note that the sulphur line ratio changes lightly with  $q$ . This effect is caused by the fact that critical densities are mildly sensitive to electron

temperature. So, in general, density-sensitive line ratios are weakly dependent on electron temperature as well; lines with a higher critical density favor a higher temperature. Nebulae characterized by high ionization parameters have high average electron temperatures. This effect causes the decrease of  $[\text{S III}]/[\text{S III}]$  towards lower values with increasing ionization parameter.

The excitation potentials of  $[\text{S III}]$  and  $[\text{Ne II}]$  (23.34 eV and 21.56 eV respectively) are close enough to make the ratio almost insensitive to the hardness of the radiation field. The substantially different critical densities,  $6.1 \cdot 10^5 \text{ cm}^{-3}$  for  $[\text{Ne II}]$  and  $1.0 \cdot 10^4 \text{ cm}^{-3}$  for  $[\text{S III}]$ , make  $[\text{S III}]/[\text{Ne II}]$  very sensitive to the ISM density in the  $10^4 - 10^6 \text{ cm}^{-3}$  range (lower panel in Fig. 5). Being sensitive to a different density regime  $[\text{S III}]/[\text{Ne II}]$  is not so much a replacement for  $[\text{S III}]/[\text{S III}]$  as a density probe, but nicely complementary.

### 3.2. Age evolution of line ratios: near-infrared

If we expand towards shorter wavelengths and include the near-infrared regime in our analysis, several other useful diagnostics become available. For one, the near-infrared is rich in hydrogen and helium recombination lines. As with the mid-infrared fine-structure lines these near-infrared lines can be used as a thermometer. In a soft radiation field, there are many more photons available for the excitation of hydrogen, which has the lowest potential (13.6 eV for hydrogen versus 24.6 eV for helium), resulting in weak He I recombination lines relative to the H I lines. With an increasingly hard radiation field the helium Strömngren sphere gradually fills that of hydrogen, observable by a higher ratio, until it finally saturates when the two Strömngren spheres coincide (Fig. 5 in Thornley et al. 2000).

$\text{He I}_{2.06\mu\text{m}}/\text{Br}\gamma$  has been shown to be an unreliable diagnostic, or at least one that is very complicated to interpret (Rigby & Rieke 2004; Lumsden et al. 2001). This is because the  $\text{He I}_{2.06\mu\text{m}} 2^1\text{P} - 2^1\text{S}$  line does not purely arise from a recombination cascade. The population of the  $2^1\text{P}$  level can be affected both by collisional pumping from the metastable  $2^1\text{S}$  level as well as resonance scattering of the  $\text{He I } 2^1\text{P} - 2^1\text{S}$  transition at 584 Å. This effect makes the helium line very sensitive to nebular conditions. The  $\text{He I}_{1.70\mu\text{m}}$  originates almost exclusively from recombination cascade, making a  $\text{He I}/\text{H I}$  ratio involving this line a much cleaner diagnostic.  $\text{He I}_{1.70\mu\text{m}}$  and  $\text{H I}(10-4)$  (Brackett 10, Br10) are close in wavelength and  $\text{He I}_{1.70\mu\text{m}}/\text{Br}10$  is therefore hardly affected by reddening. This ratio has been extensively tested as stellar temperature diagnostic and found to show good agreement with other temperature indicators (Rigby & Rieke 2004). Unfortunately, the  $\text{He I}_{1.70\mu\text{m}}$  line is relatively faint, less than one-tenth of the  $\text{Br}\gamma$  intensity. This means it can usually only be detected in nearby objects with very bright recombination lines.

*Mappings* does not predict the intensity of either the  $\text{He I } 2.06$  or the  $1.70 \mu\text{m}$  line. To obtain the  $\text{He I } 1.70 \mu\text{m}$  line strength we therefore scale the  $\text{He I } 4471 \text{ Å}$  line, which originates from the same upper level. Under the assumption of case B recombination and for the full range of temperatures and densities examined here the  $4471 \text{ Å}$  line has to be scaled by  $6.6 \cdot 10^{-2}$  (Benjamin et al. 1999).

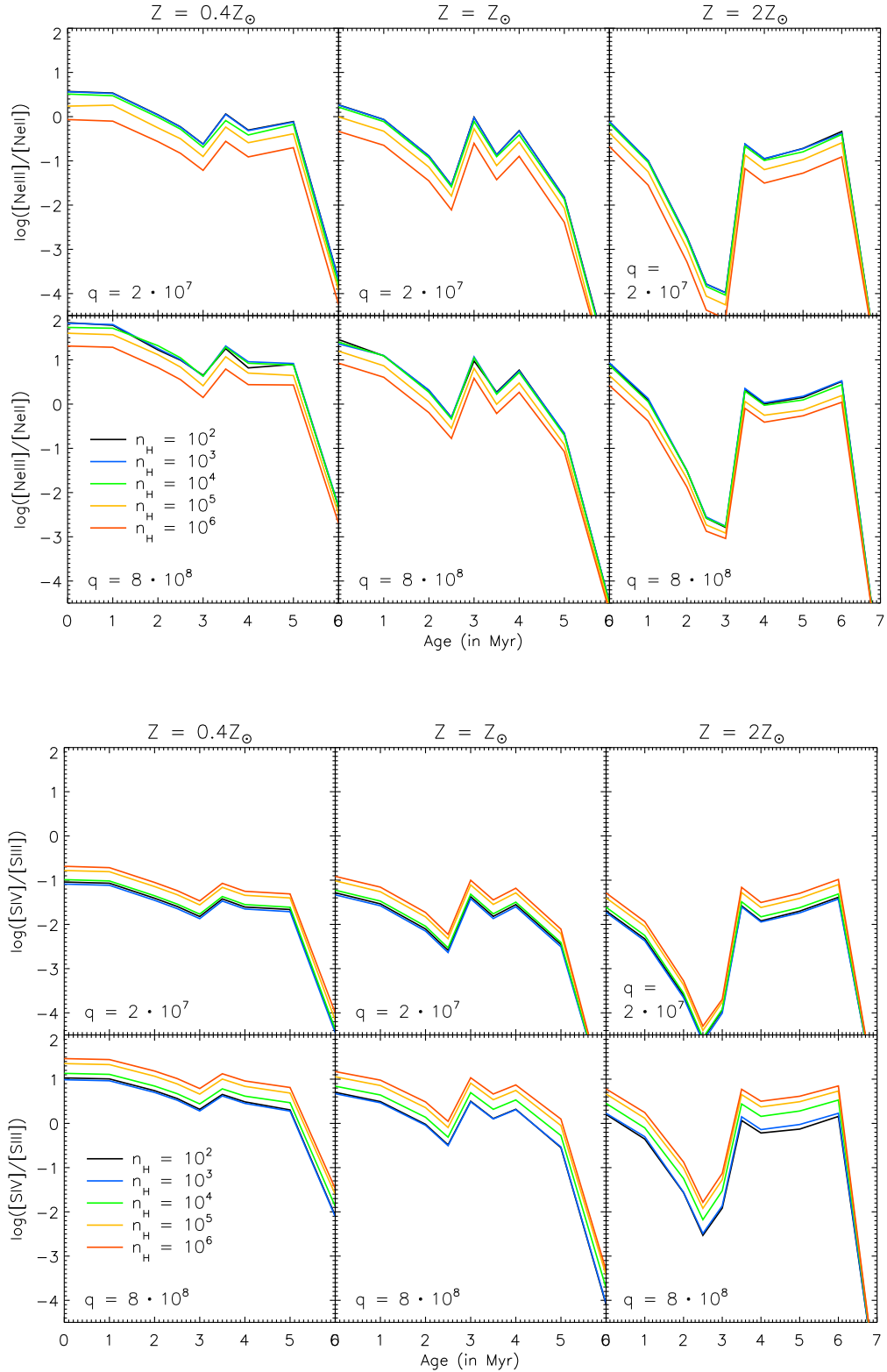


FIG. 4.— Evolution of the emission line ratios with cluster age of *upper*:  $[NeIII]_{15.56\mu m}/[NeII]_{12.81\mu m}$  and *lower*:  $[SIV]_{10.51\mu m}/[SIII]_{18.71\mu m}$ . The left panels show the curves for  $Z = 0.4Z_{\odot}$ , the middle panels  $Z = Z_{\odot}$  and the right panels  $Z = 2Z_{\odot}$ . The upper row shows the case of low ionization parameter,  $q = 2 \cdot 10^7$   $\text{cm}^{-1}$ , the lower row that of high ionization parameter,  $q = 8 \cdot 10^8$   $\text{cm}^{-1}$ . Curves of different line style (different color in electronic edition) represent results of models with different densities, ranging from  $10^2$   $\text{cm}^{-3}$  to  $10^6$   $\text{cm}^{-3}$ . Line ratio values can be found tabulated at [www.ifa.hawaii.edu/~kewley/Mappings/IRdiagnostics](http://www.ifa.hawaii.edu/~kewley/Mappings/IRdiagnostics).

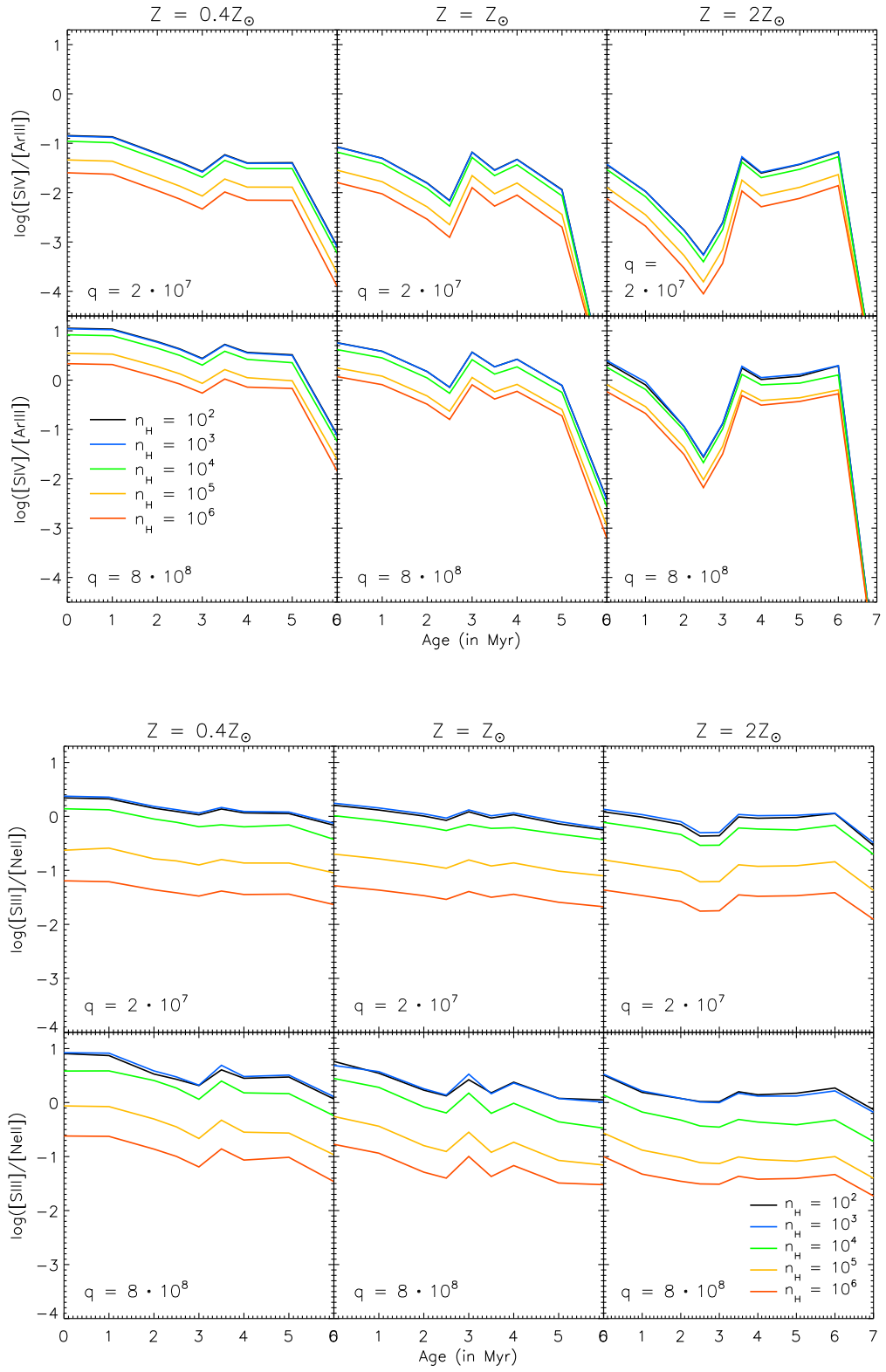


FIG. 5.— Like Fig. 4 for *upper*:  $[SIV]_{10.51\mu m}/[ArIII]_{8.99\mu m}$  and *lower*:  $[SIII]_{18.71\mu m}/[NeII]_{12.81\mu m}$ .

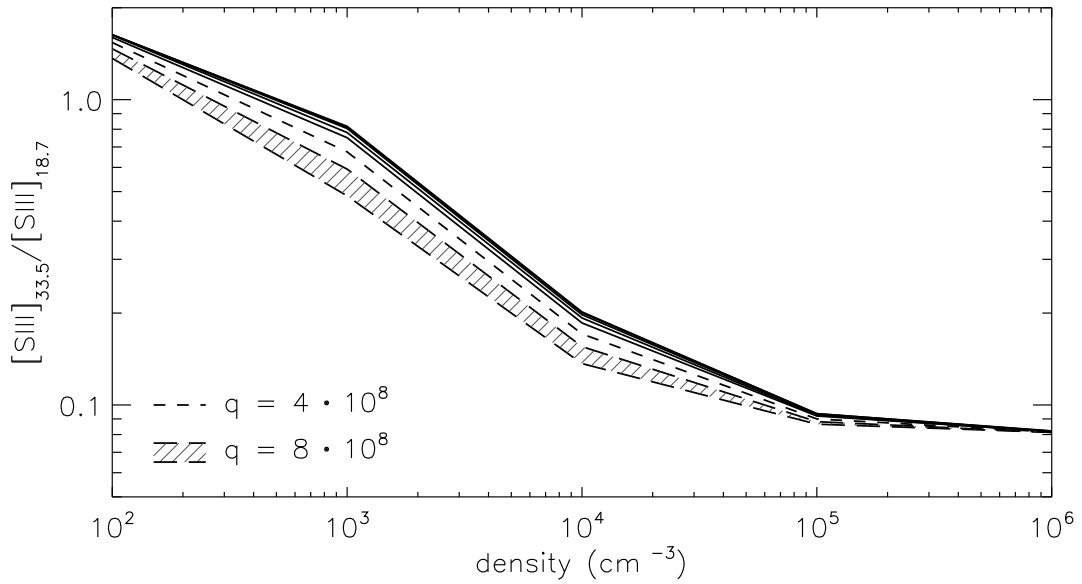


FIG. 6.— Evolution of the  $[\text{S III}]_{33.48\mu\text{m}}/[\text{S III}]_{18.71\mu\text{m}}$  ratio with increasing density. The solid lines result from the models with an ionization parameter of  $2 \cdot 10^7$ ,  $4 \cdot 10^7$ ,  $8 \cdot 10^7$  and  $1.6 \cdot 10^8$   $\text{cm s}^{-1}$  (top to bottom solid line, the  $2 \cdot 10^7$  and  $4 \cdot 10^7$  are indistinguishable). For a higher ionization parameter the curve drops towards somewhat lower  $[\text{S III}]/[\text{S III}]$  values (short-dashed line:  $4 \cdot 10^8$   $\text{cm s}^{-1}$ ; long-dashed line:  $8 \cdot 10^8$   $\text{cm s}^{-1}$ ; the shaded area connects the  $q = 8 \cdot 10^8$   $\text{cm s}^{-1}$  curves of different ages, the upper curve represents the average values for 0 – 4 Myr and the lower curve shows the 5 Myr values). The differences between the curves is caused by a weak dependence of the  $[\text{S III}]/[\text{S III}]$  ratio on electron temperature (see Section 3.1 for explanation). Line ratio values can be found tabulated at [www.ifa.hawaii.edu/~kewley/Mappings/IRdiagnostics](http://www.ifa.hawaii.edu/~kewley/Mappings/IRdiagnostics).

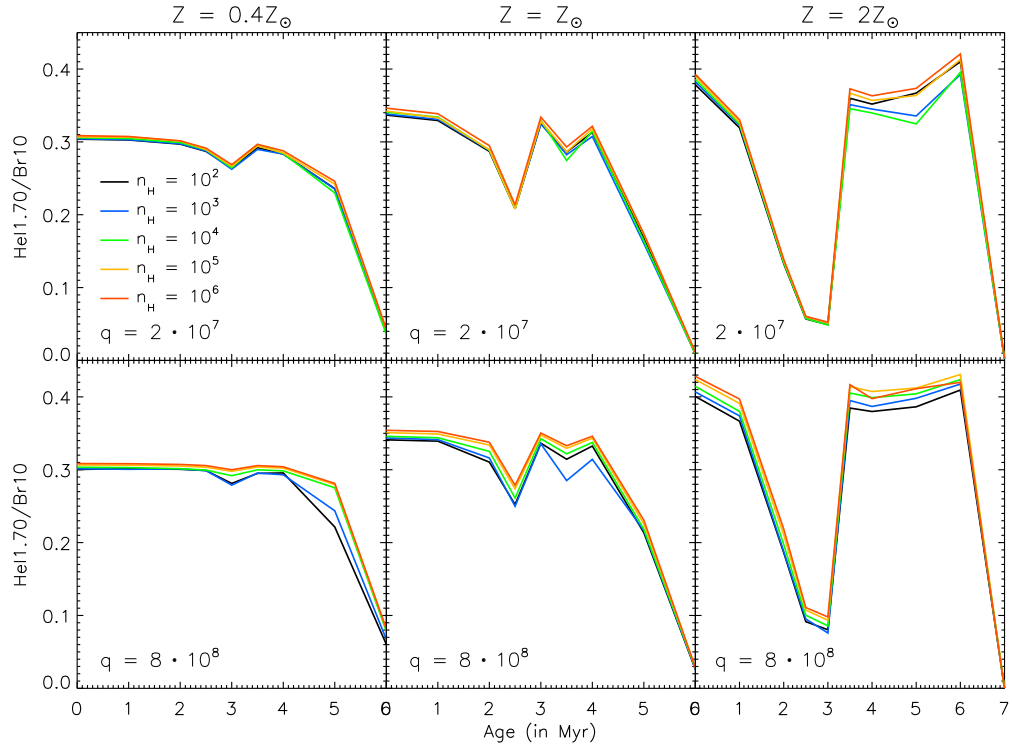


FIG. 7.— Like Fig. 4 for  $\text{He I}_{1.70\mu\text{m}}/\text{Br10}$ .

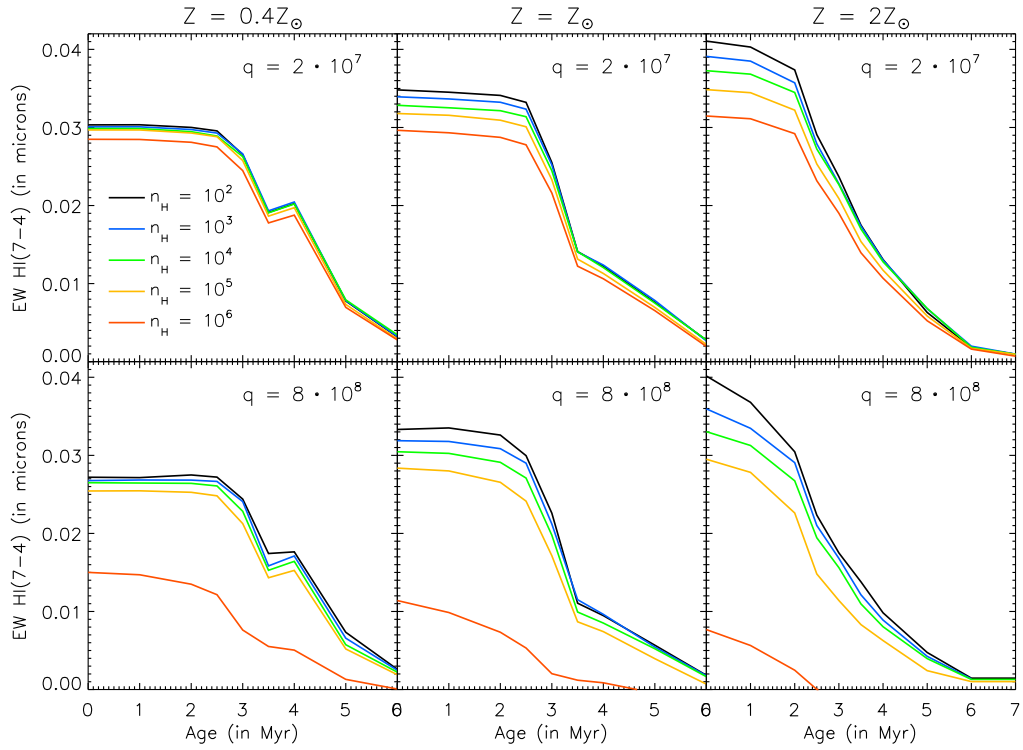


FIG. 8.— Age evolution of the equivalent width of the hydrogen recombination line  $\text{Br}\gamma$ . The left panels show the curves for  $Z = 0.4Z_{\odot}$ , the middle panels  $Z = Z_{\odot}$  and the right panels  $Z = 2Z_{\odot}$ . The upper row shows the case for low ionization parameter,  $q = 2 \cdot 10^7 \text{ cm s}^{-1}$ , the lower row that of high ionization parameter,  $q = 8 \cdot 10^8$ . Curves of different line style (different color in electronic edition) represent results of models with different density, ranging from  $10^2 \text{ cm}^{-3}$  to  $10^6 \text{ cm}^{-3}$ . Line ratio values can be found tabulated at [www.ifa.hawaii.edu/~kewley/Mappings/IRdiagnostics](http://www.ifa.hawaii.edu/~kewley/Mappings/IRdiagnostics).

The age evolution tracks of  $\text{He}_{1.70\mu\text{m}}/\text{Br}10$  are flat at the youngest ages (for  $0.4Z_{\odot}$  and  $Z_{\odot}$ ), where the ratio is saturated and the Strömgren spheres are both maximally filled (Fig. 7). With the incoming radiation field softening as the cluster ages, we see the  $\text{He}_{1.70\mu\text{m}}/\text{Br}10$  ratio drop again in a similar manner to the mid-infrared line ratios. The age evolution curves altogether have a very similar shape as the mid-infrared curves, showing the W-R phase upturn and the rapid decrease when the W-R stars disappear around 6/7 Myr. The ratio is also mildly sensitive to density because of the presence of dust in our models. When the density increases the dust competes more effectively with the gas for FUV photons. The age evolution curves do not show equally smooth behavior as those of the previously discussed mid-infrared ratios, especially at the  $2Z_{\odot}$  W-R plateau between 3.5 and 6 Myr. This is most likely the result of numerical effects in the radiative transfer of helium in the *Mappings* code.

Another commonly used near-infrared diagnostic is the equivalent width (EW) of one of the hydrogen lines as age estimator, usually the bright ones like  $\text{Pa}\beta$  in the J band or  $\text{Br}\gamma$  in K. The equivalent width measures the strength of the short-lived line emission from the young, most massive stars relative to the continuum emission from lower mass stars. Under the assumption of an instantaneous burst of star formation, the EW drops with time (EW( $\text{Br}\gamma$ ) is shown in Fig. 8). The  $Z_{\odot}$  and  $2Z_{\odot}$  curves drop monotonically, but in the low metallicity case the curve shows a small jump between 3.5 and 4 Myr, correlated with the W-R phase. With fewer heavy elements in the low metallicity W-R star atmospheres, not a lot of ionizing photons are absorbed in the process of line-blanketing and most are available for the ionization of the surrounding matter. These ionizing photons boost the hydrogen line fluxes. In the (super)solar metallicity case, where a lot of the ionizing photons are used to ionize the W-R star atmospheres, this upturn in the EW of  $\text{Br}\gamma$  is not observed. The decreasing value of the EW with increasing density reflects the dusty nature of our models in the same way as discussed for  $\text{He}_{1.70\mu\text{m}}/\text{Br}10$ . For all but the most extreme case this results in a spread of less than 33% in the value of EW( $\text{Br}\gamma$ ). Only the models with an ionization parameter  $q$  of  $8 \cdot 10^8$  in combination with a density  $n_H$  of  $10^6 \text{ cm}^{-3}$  show very distinct values. The dust becomes the dominant absorber of Lyman continuum photons in these most extreme models.

#### 4. COMPARISON WITH EXISTING MID-INFRARED MODELS

Both Rigby & Rieke (2004) and Martín-Hernández et al. (2005) (hereafter RR04 and MH05 respectively) have performed similar studies to this work, but covering a more limited range of parameter space, assuming average values for parameters such as density and ionization parameter. In both works the age evolution of several line ratios was calculated in a comparable way to that presented here, using *Starburst 99* in combination with the photoionization code *Cloudy* (Ferland 2001, RR04 used *Cloudy* version 94.00, MH05 version 96.00-beta 4). Both assume stellar populations with a Salpeter IMF between  $1 M_{\odot}$  and

various upper mass-cutoffs (RR04: 30, 40, 50, 60, 75 &  $100 M_{\odot}$  and MH05: 30, 50 &  $100 M_{\odot}$ ), exploring a range of sub-solar and solar metallicities. The models of RR04 are characterized by an ionization parameter of  $\log U = -2.3$  ( $q = 1.37 \cdot 10^8 \text{ cm s}^{-1}$ ) and a density of  $300 \text{ cm}^{-3}$ . MH05 fix the density at  $5 \cdot 10^4 \text{ cm}^{-3}$ . The ionization parameter for their object (NGC 5253) is estimated to be at least  $\log U = -0.5$  ( $q = 8.62 \cdot 10^9 \text{ cm s}^{-1}$ ).

To accurately compare our models to those of RR04 and MH05, we ran a set of models with identical parameters (solar metallicity,  $q = 1.37 \cdot 10^8$ , and  $n_H = 300 \text{ cm}^{-3}$  for RR04, and solar metallicity,  $q = 8.62 \cdot 10^9 \text{ cm s}^{-1}$  and  $n_H = 5 \cdot 10^4 \text{ cm}^{-3}$  for MH05). The resulting ratios of various emission lines are plotted as a function of age in Fig. 9. As judged from the age evolution of  $\text{He}_{1.70\mu\text{m}}/\text{Br}10$  (upper row in Fig. 9), the temperature evolution of the RR04 models is very similar to ours. The curves for this line ratio essentially coincide. The mid-infrared line ratios of our models are considerably different. Quantitatively the overall shape of the curves is similar, with an initial drop and an upturn corresponding to the W-R phase. However, the onset of the W-R phase happens earlier in our models and the relative strength of the upturn is different; the W-R stars do not seem to produce an equally hard radiation field in the RR04 models as they do in ours. Since the discrepancy between the two sets of models is largest during the W-R phase, we expect the modeling of the W-R stellar atmospheres in *Starburst 99* to be (partly) responsible for the differences. And although both studies use the same atmospheric libraries, the treatment of W-R stars seem to have changed between *v4.0* (used by RR04) and *v5.1* (used in our work). Furthermore, there is a significant difference in the modeling of the surrounding nebula. We include dust, while RR04 model a purely gaseous nebula. The dust competes with the gas for ionizing photons, which will significantly alter the ionization structure within the nebula. There are most probably computational differences between *Mappings* and *Cloudy* as well, and differences in the assumed value for the abundances, like sulphur over hydrogen (S/H) (the abundance set is not given in RR04).

In the lower row of panels in Fig. 9 we compare our model results to those of MH05. The general shape of the age evolution curves of MH05 shows a better agreement with our model results than RR04. However, the agreement between the values of the  $[\text{Ne III}]/[\text{Ne II}]$ ,  $[\text{S IV}]/[\text{Ne II}]$  and  $[\text{Ar III}]/[\text{Ne II}]$  line ratios produced by our models and those of MH05 is worse, with those of MH05 often over an order of magnitude larger. This difference most probably arises from differences in the geometry applied. We model the gas and dust as a thin slab (the thickness of the slab is much smaller than the distance from the radiating source to the slab's inner radius) and MH05 adopt a spherical model with a relatively thick shell of gas and dust around the stellar cluster (inner radius is 0.6 pc, outer radius is 0.8 pc). Because of this geometrical difference, the cloud in the MH05 model sees an intenser UV field at the inner cloud radius for identical cloud parameters. This results in large differences in predicted mid-IR emission line ratios.

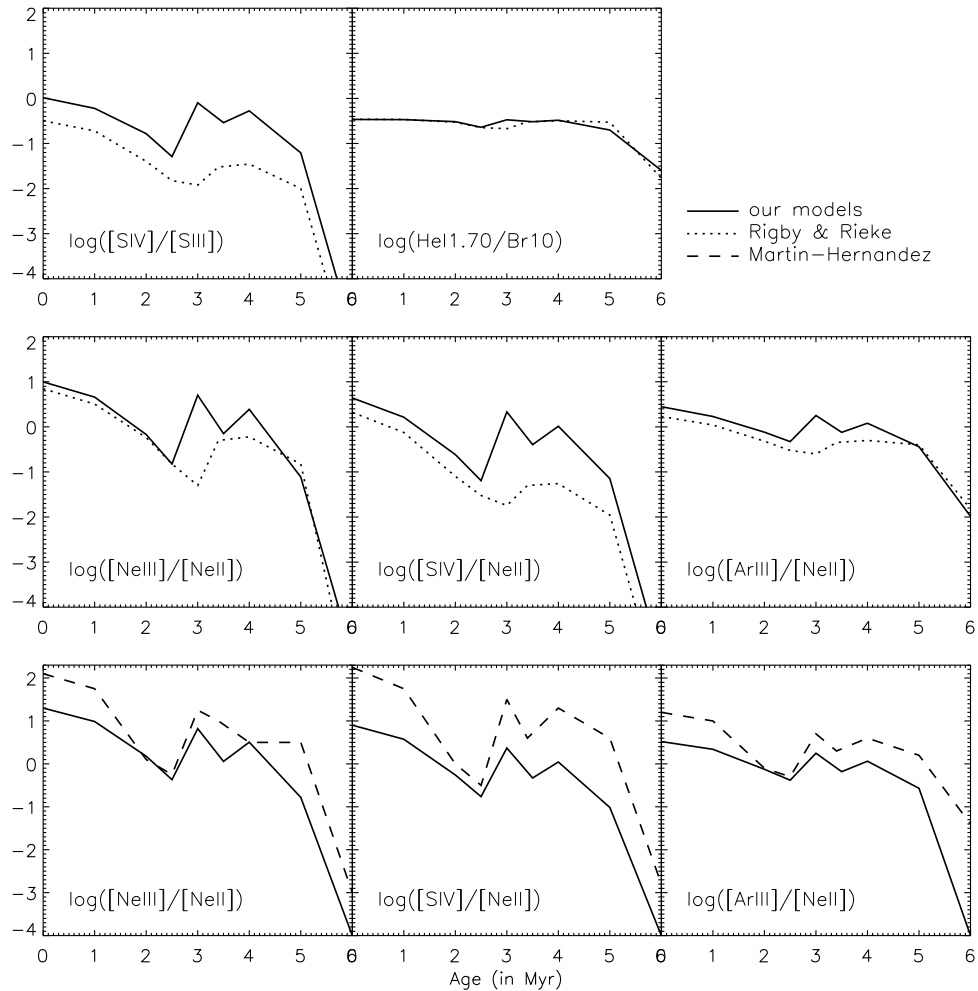


FIG. 9.— Comparison of results for the age evolution of various emission line ratios of our models (solid lines) with results of RR04 (dotted line in the top and middle row of panels) and with results of MH05 (dashed line in panels in the bottom row). The solid lines (our model results) and the dotted curves (RR04) in the top and middle row of panels can be characterized by  $Z = Z_{\odot}$ ,  $n_H = 300 \text{ cm}^{-3}$  and  $q = 1.37 \cdot 10^8 \text{ cm s}^{-1}$ . The solid lines and the dashed lines in the lowest row of panels show our model results and those of MH05 for  $Z = Z_{\odot}$ ,  $q = 8.62 \cdot 10^9 \text{ cm s}^{-1}$  and  $n_H = 5 \cdot 10^4 \text{ cm}^{-3}$ .

## 5. DIAGNOSTIC DIAGRAMS

To construct more powerful diagnostic tools, we combine various line ratios into ratio–ratio plots. Figure 10 shows the age evolution of  $[SIV]/[SIII]$  versus  $[NeIII]/[NeII]$  as a function of metallicity, density and ionization parameter.

Fig. 4 already showed that  $[SIV]/[SIII]$  and  $[NeIII]/[NeII]$  both measure the hardness of the radiation in a similar way and show very comparable age evolution tracks. Therefore the curves run nicely parallel and behave very orderly in the diagnostic diagram. Note however that at ages  $\geq 3$  Myr the metallicity curves wrap around each other, introducing a metallicity–spectral hardness degeneracy. This effect is caused by the difference in sensitivity of the ratios to radiation hardness. At this age the evolution curves in Fig. 4 change rapidly and are substantially different for

each metallicity, causing the metallicity curves in the diagnostics diagram in Fig. 10 to fold.

The age evolution curves of  $[SIV]/[ArIII]$  and  $[SIII]/[NeII]$  differ considerably in shape (Fig. 5), causing the curves in the ratio–ratio plot to look much more complex than the ones in the diagram discussed in the previous paragraph. Different behavior from the  $[NeIII]/[NeII]$  to  $[SIV]/[SIII]$  is expected, since here we plot a hardness-sensitive ratio,  $[SIV]/[ArIII]$ , versus a ratio that is mainly sensitive to density,  $[SIII]/[NeII]$  (Fig. 11). The fact that  $[SIII]/[NeII]$  is almost exclusively affected by density and not so much by radiation hardness causes the relatively small spread in  $[SIII]/[NeII]$  values within each individual panel. As in the  $[NeIII]/[NeII]$  to  $[SIV]/[SIII]$  diagram the metallicity curves wrap around each other at ages  $\geq 3$  Myr to form an interwoven knot of model points that are not easily

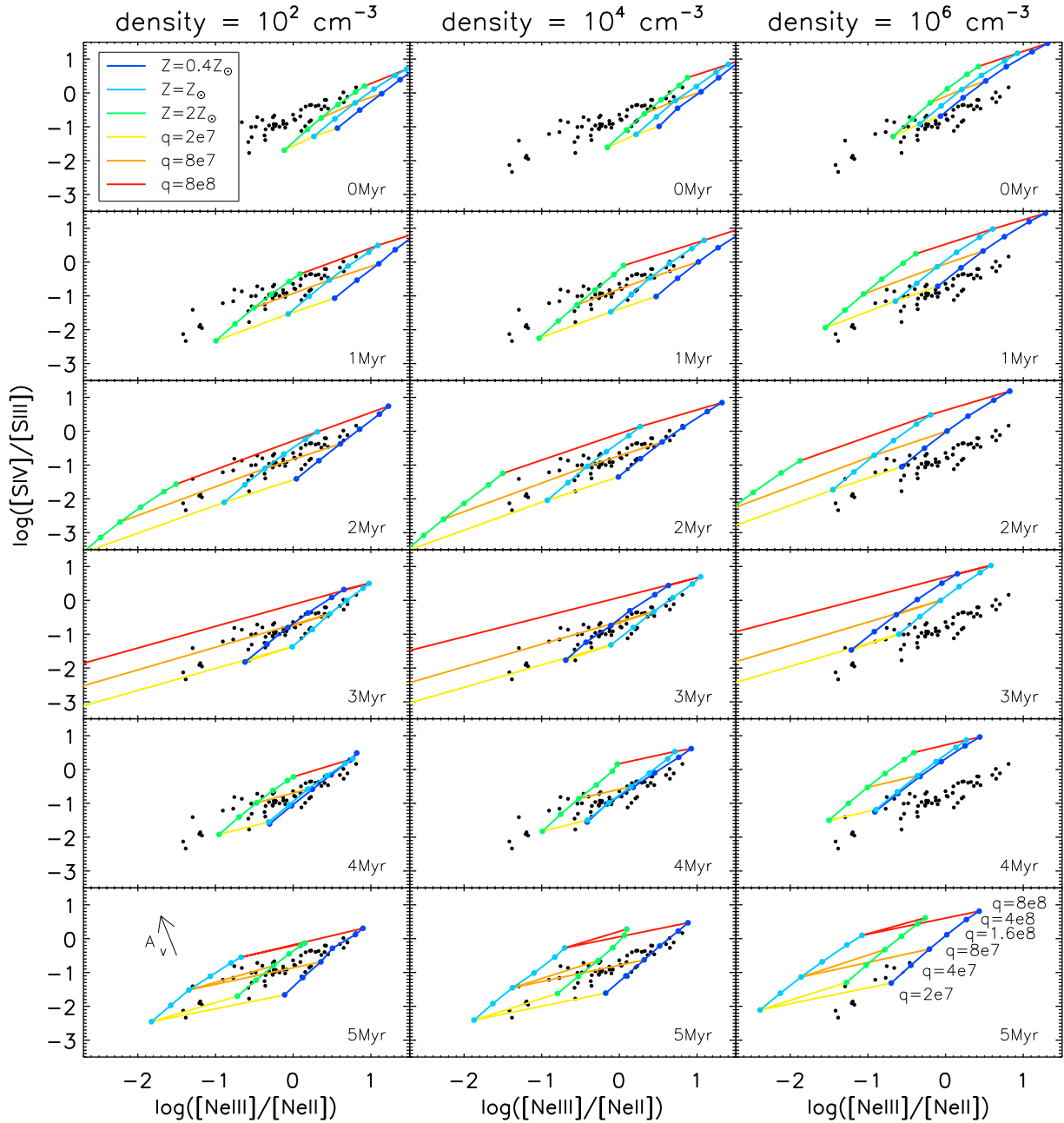


FIG. 10.—  $[\text{SIV}]/[\text{SIII}]$  versus  $[\text{NeIII}]/[\text{NeII}]$  as a function of metallicity, density and ionization parameter. Stepping down from the top to the bottom panels the plots show the age evolution of the ratios in 1 Myr steps. The left column shows the lowest density case,  $n_H = 10^2 \text{ cm}^{-3}$ , the middle column intermediate density,  $n_H = 10^4 \text{ cm}^{-3}$  and the right column shows the very dense case,  $n_H = 10^6 \text{ cm}^{-3}$ . Within every individual panel, the blue/green curves represent the different metallicities; dark blue corresponds to  $Z = 0.4Z_\odot$ , light blue to  $Z = Z_\odot$  and green to  $Z = 2Z_\odot$ . The dots overplotted in the metallicity curves relate to the various values for the ionization parameter  $q$ , with the lowest point corresponding to  $q = 2 \cdot 10^7 \text{ cm s}^{-1}$  and the topmost point to  $q = 8 \cdot 10^8 \text{ cm s}^{-1}$ . All individual steps in  $q$  value are indicated in the bottom-right panel. The points for  $q = 2 \cdot 10^7 \text{ cm s}^{-1}$  are connected by a yellow line, the points for  $q = 8 \cdot 10^7 \text{ cm s}^{-1}$  by an orange and those for  $q = 8 \cdot 10^8 \text{ cm s}^{-1}$  by a red line. Note that the metallicity curves start wrapping around each other  $\geq 3$  Myr. The black dots are measurements of galactic HII regions (Giveon et al. 2002). Data points indicating upper limits are excluded from this and the following plot to avoid confusion. The arrow in the bottom-left panel indicates an  $A_V$  of 50. Line ratio values can be found tabulated at [www.ifa.hawaii.edu/~kewley/Mappings/IRdiagnostics](http://www.ifa.hawaii.edu/~kewley/Mappings/IRdiagnostics).

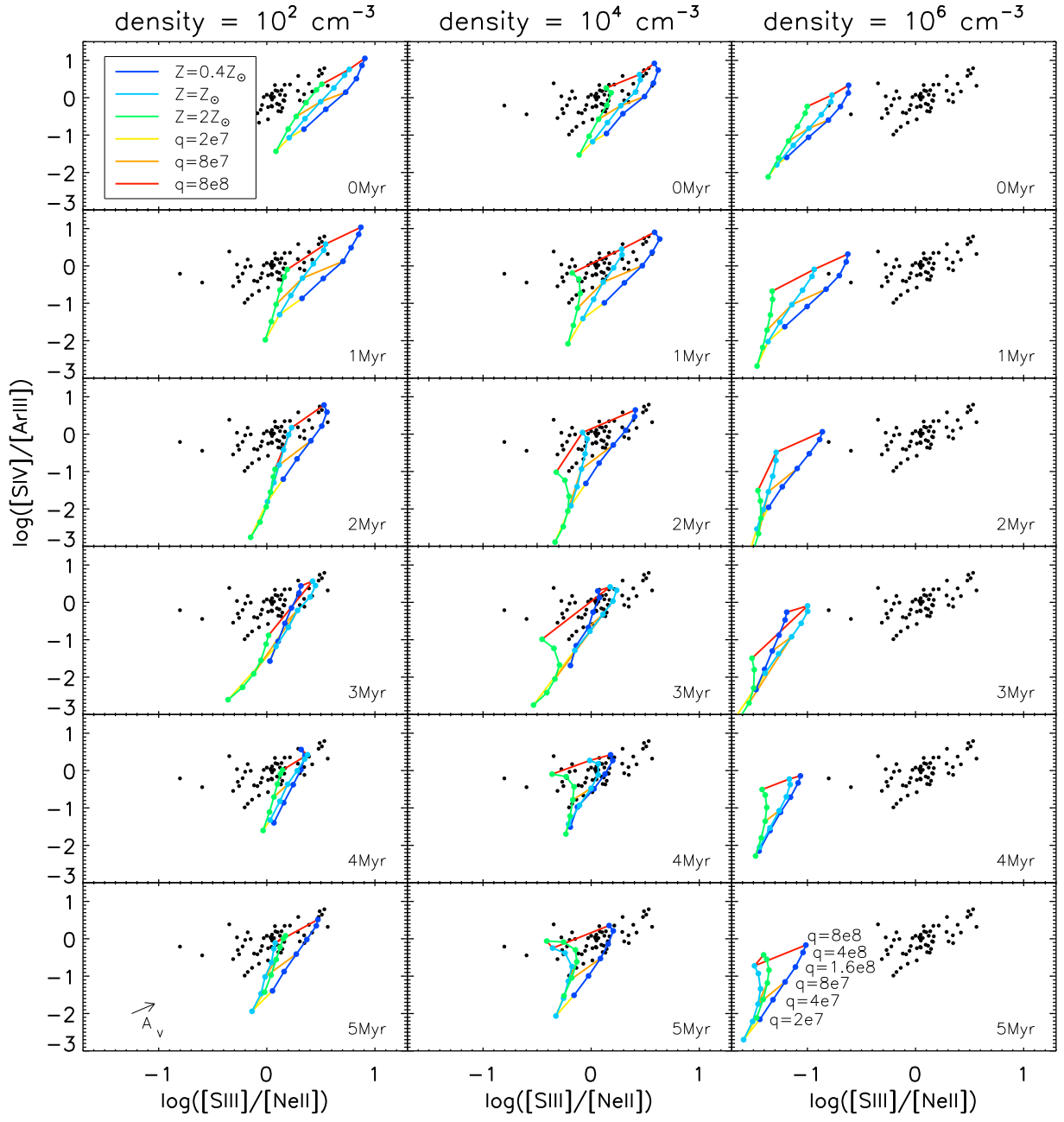


FIG. 11.— As Fig. 10 for  $[\text{SIV}]/[\text{Ar III}]$  versus  $[\text{SIII}]/[\text{Ne II}]$ . The arrow in the bottom-left panel indicates an  $A_V$  of 100.

distinguished.

## 6. COMPARISON WITH PUBLISHED DATA

To test the model results, we compare the model output with mid-infrared data of galactic and extragalactic H II regions published by Giveon et al. (2002). This data set consists of a sample of 149 H II regions; 112 galactic H II regions, 14 H II regions in the Large Magellanic Cloud (LMC), 4 in the Small Magellanic Cloud (SMC) and 19 in M33. From the ISO archive, the authors selected all H II regions that are bright in one of the neon fine-structure lines and for which both observations in low-resolution full spectrum mode (Short Wavelength Spectrometer; SWS01) as well as in medium-resolution line spectroscopy mode (SWS02) were available. The final spectra cover the wavelength range of 2.4 – 45  $\mu\text{m}$  with a spectral resolution  $r = 400$  (low resolution) - 2000 (medium-resolution). Since these observations originate from numerous different projects, all with their own distinctive research goals, the final sample is very heterogeneous. It contains many regular star-forming regions as well as very bright and/or compact H II regions. This broad range of conditions tests the ability of our model grid to reproduce a large variety of different H II region properties.

The data points of the H II regions are plotted in the diagnostic diagrams presented in the previous section (Figs. 10 and 11). In Fig. 10 we see that the models and data agree very well in general, occupying the same range in the ratio–ratio values. The data points follow a distribution that is somewhat tilted compared to the lines of equal ionization parameter, most probably reflecting morphological differences between the individual regions, resulting in variations in the ionization parameter. The horizontal spread exhibits a range in metallicities and densities. In general, the highest density models do not do as well explaining the data as the low and intermediate density models do. Furthermore, the very youngest age of 0 Myr can be ruled out for most data points. On average the H II data indicate an age for the star-forming regions  $\geq 1$  Myr and an intermediate ionization parameter ( $4 \cdot 10^7 \text{ cm s}^{-1} \leq q \leq 1.6 \cdot 10^8 \text{ cm s}^{-1}$ ).

Examining Fig. 11 shows that here again the data points and models overlap nicely, although in this diagram there are a handful of points displaying ratio–ratio values that are not covered by the model grid, mainly at the high ionization end. It is quite clear that a density of  $10^6 \text{ cm}^{-3}$  is too high for all data points (but one). On average the intermediate density model curves ( $10^4 \text{ cm}^{-3}$ ) cover a significant fraction of the data points, but all densities ranging from  $10^2$  to  $10^5 \text{ cm}^{-3}$  are capable of reproducing the data. The mean ionization parameter indicated by this diagram is higher than concluded from the previous diagram, for most data a value of  $q$  between  $8 \cdot 10^7$  and  $8 \cdot 10^8 \text{ cm s}^{-1}$  is required.

## 7. A TEST CASE FROM THE GROUND: STELLAR CLUSTERS IN THE OVERLAP REGION OF THE ANTENNAE

To address the diagnostics based on the spectral features that are accessible from the ground only, we use infrared data of young stellar clusters in the Antennae overlap region as a test case. We combine

near-infrared Infrared Spectrometer And Array Camera (ISAAC) at the VLT (Moorwood et al. 1998) with mid-infrared VLT Imager and Spectrometer for mid Infrared (VISIR, Lagage et al. 2004) spectra.

The overlap region of the Antennae, the region of interaction between the two merging spiral galaxies, is known from mid-infrared observations to host the most active sites of star formation, some severely reddened by the presence of massive amounts of dust. Based on ISO observations Mirabel et al. (1998) concluded that 15% of the total mid-infrared flux at 15  $\mu\text{m}$  of the whole NGC 4038/4039 system originates from a deeply embedded, off-nuclear star-forming region, corresponding to a faint, very red cluster in the optical (source 80 in Whitmore & Schweizer 1995). The clusters under study are this highly reddened cluster and an optically bright, blue cluster complex, which is the counterpart of the second brightest infrared source in the overlap region. The source IDs are 1a and 2 in Snijders et al. (2006) for the reddened cluster and the cluster complex respectively, corresponding to the bright near-infrared sources ID<sub>WIRC</sub> 157 and ID<sub>WIRC</sub> 136 (Brandl et al. 2005).

### 7.1. Observations, data reduction and results

The southern part of the overlap region of NGC4038/39 was observed with VISIR. Low-resolution N band spectra of the two brightest sources in the mid-infrared were already published in Snijders et al. (2006). Additionally, medium-resolution spectroscopy around the [S III] line at 18.71  $\mu\text{m}$  was obtained for the same two sources. The total on-source integration time for these observations was 80 minutes. The same setup was used as with the N band observations, applying chopping and nodding on-slit with a 10'' chopper throw. HD93813 was observed before and after the observation for flux calibration (Cohen et al. 1999). The data were reduced in the same way as the N band spectra and data were extracted in a 1.''27 aperture ( $\approx 133 \text{ pc}$  at a distance of 21 Mpc<sup>1</sup>, assuming a Hubble constant of 70 km s<sup>-1</sup> Mpc<sup>-1</sup>; at this distance 1'' corresponds to 105 pc).

Absolute flux calibration was obtained by normalizing the standard star spectrum to VISIR narrow-band fluxes. The accuracy of the flux calibration is 20%. Figure 12 shows the resulting Q band spectra.

For our analysis we use the N and Q band emission lines, and additionally the flux ratio of He I<sub>1.70 $\mu\text{m}$</sub> /Br10 from the H band and the EW(Br $\gamma$ ) from K<sub>s</sub> band spectra, both obtained with ISAAC (Snijders & Van der Werf, in preparation). For the near-infrared observations the on-source integration time was 20 minute in each spectroscopic setting. The spectra were extracted in 3.''5 apertures. This aperture is considerably larger than the aperture applied on the mid-infrared data. We have done so to capture all the hydrogen emission line flux that can be associated with the clusters and to compensate for a worse seeing in the near- compared to the mid-infrared.

The data were extinction corrected assuming a standard Draine (1989) extinction curve. We obtained estimates for the visual extinction  $A_V$  from Mengel et al.

<sup>1</sup> Note that the distance of the Antennae is under debate. Recently a lower distance of  $13.8 \pm 1.7 \text{ Mpc}$  was found (Saviane et al. 2004), which would affect the values derived here.

TABLE 2  
NEAR- AND MID-INFRARED DATA OF STAR CLUSTERS IN THE ANTENNAE OVERLAP REGION

Species	Wavelength ( $\mu\text{m}$ )	Source 1a <sup>a</sup>		Source 2 <sup>b</sup>	
		measured	ext corr <sup>c</sup>	measured	ext corr <sup>c</sup>
Br $\gamma$ <sup>d</sup>	2.166	$1.4 \pm 0.2$	$2.1 \pm 0.2$	$1.5 \pm 0.2$	$1.5 \pm 0.2$
EW(Br $\gamma$ ) <sup>e</sup>	2.166	$3.6 \pm 0.4$	$3.6 \pm 0.4$	$2.8 \pm 0.3$	$2.8 \pm 0.3$
He I <sub>1.70<math>\mu\text{m}</math></sub> /Br10	1.700/1.737	$0.309 \pm 0.046$	$0.315 \pm 0.047$	$0.299 \pm 0.045$	$0.299 \pm 0.045$
[Ar III] <sup>d</sup>	8.99	$3.9 \pm 0.9$	$5.9 \pm 1.4$	$4.2 \pm 0.7$	$4.3 \pm 0.7$
[S IV] <sup>d</sup>	10.51	$7.6 \pm 0.9$	$11.8 \pm 1.4$	$10.3 \pm 2.3$	$10.6 \pm 2.4$
[Ne II] <sup>d</sup>	12.81	$49.6 \pm 6.2$	$59.8 \pm 7.5$	$30.2 \pm 4.5$	$30.6 \pm 4.6$
[S III] <sup>d</sup>	18.71	$31.2 \pm 3.8$	$38.4 \pm 4.7$	$38.3 \pm 3.9$	$38.8 \pm 4.0$

<sup>a</sup> ID<sub>WIRC</sub> 157 in Brandl et al. (2005), cluster 80 in Whitmore & Schweizer (1995)

<sup>b</sup> ID<sub>WIRC</sub> 136 in Brandl et al. (2005), star-forming knot B in Whitmore et al. (2005)

<sup>c</sup>  $A_V$  is 4.23 for source 1a and 0.28 for source 2

<sup>d</sup> line fluxes in  $10^{-14}$  erg s<sup>-1</sup> cm<sup>-2</sup>

<sup>e</sup> equivalent width in  $10^{-2}$   $\mu\text{m}$

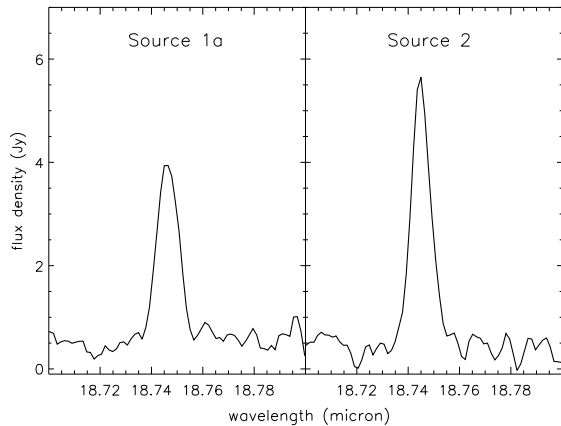


FIG. 12.— Medium-resolution Q band spectroscopy of the 18.71  $\mu\text{m}$  [S III] emission-line for *left*: source 1a, and *right*: source 2.

(2005). These values for the extinction were derived from the ratio of the near-infrared hydrogen recombination lines H $\alpha$  and Br $\gamma$ . For source 1a there was only one possible near-infrared counterpart, for which an  $A_V$  of 4.23 was determined. For source 2 we selected all sources within an  $1''.4$  radius, resulting in four possible near-infrared counterparts. To correct source 2 for extinction we use the average  $A_V$  value of these four sources,  $A_V = 0.28$  (the spread in values for  $A_V$  was  $0.16 - 0.42$ ). Table 2 lists the mid-infrared emission line fluxes and the EW(Br $\gamma$ ) and He I<sub>1.70 $\mu\text{m}$</sub> /Br10 from the near-infrared spectra.

The resulting mid-IR data points are compared with the sample of H II regions observed in our and other nearby galaxies (the data set presented in Section 6). Fig. 13 shows that the Antennae clusters fall within the general distribution of H II regions, though right at the edge.

The cluster ages are constrained using the EW(Br $\gamma$ ) (see Fig. 14). Source 1a has the highest value for EW(Br $\gamma$ ) and its age must be 2.5 Myr or younger. Furthermore, the metallicity of this source must be around solar or higher, since the  $0.4Z_\odot$  cannot reproduce the observed value for EW(Br $\gamma$ ). The age of source 2 falls in the range of 0 – 3 Myr. For this source it is not possible to discriminate between the different metallicities. Taking these age constraints into account, it is clear from

the [S IV]/[Ar III] versus [S III]/[Ne II] diagnostic diagram (Fig. 15) that the highest density models, with a  $n_H$  of  $10^6$  cm<sup>-3</sup>, disagree with the data points. In general the medium density curves ( $n_H = 10^4$  cm<sup>-3</sup>) come closest to the data. Both clusters require a very high ionization parameter, the data points occupy an area in the ratio-ratio plot that is characterized by a value of  $q \geq 8 \cdot 10^8$  cm s<sup>-1</sup>. Further implications are discussed in Sections 8.2 and 8.3.

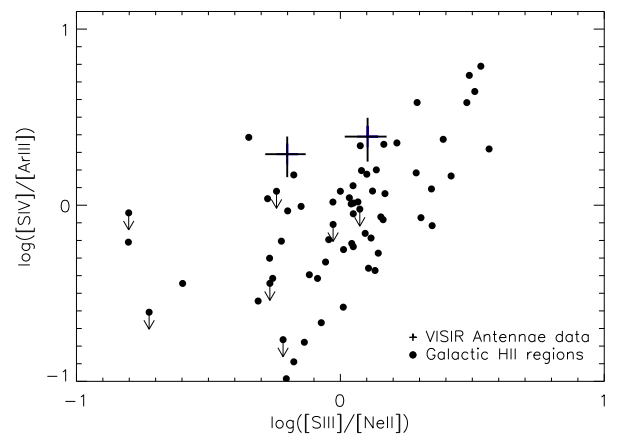


FIG. 13.— Comparison of the [S IV]/[Ar III] and [S III]/[Ne II] ratio of the Antennae clusters observed with VISIR (crosses, this work) with (extra-)galactic H II regions (dots: Givon et al. 2002). None of the data is extinction corrected. The Antennae data points include error bars.

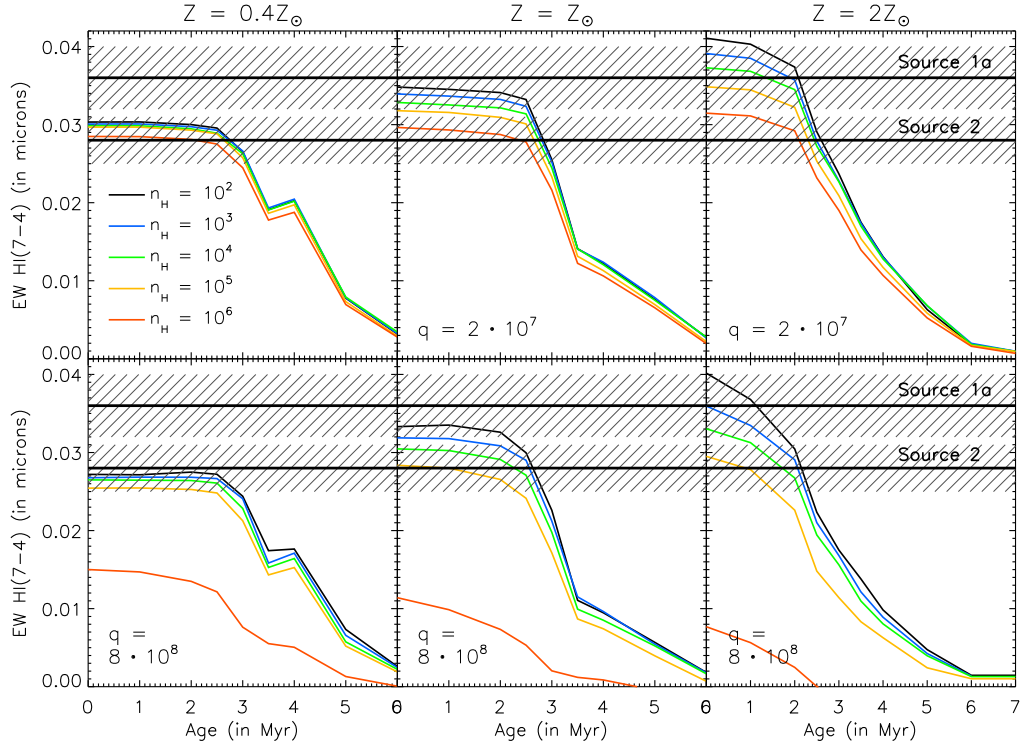


FIG. 14.— This plot is identical to Fig. 8 with the data points for the Antennae clusters included. The fat black line indicates the value of  $\text{EW}(\text{Br}7)$  for both sources as measured from ISAAC spectra. Error bars are indicated by the shaded areas. From this plot we conclude that both clusters are young, source 1a  $\leq 2.5$  Myr and source 2  $\leq 3$  Myr.

## 8. DISCUSSION

### 8.1. Modeling infrared line emission of young star-forming regions

The model grid presented in this paper covers a large range in metallicities, gas densities and ionization parameters to mimic the characteristics of all kinds of star-forming regions. Testing the model output with galactic and extragalactic (UC)H II regions shows that the models succeed in reproducing the mid-infrared characteristics of objects with a wide range of properties, from diffuse H II to UCH II regions as well as starburst nuclei. There is a very good agreement between the observed ratio-ratio values, like  $[\text{SIV}]/[\text{SIII}]$  versus  $[\text{NeIII}]/[\text{NeII}]$ , and the range in values predicted by the models.

We do not encounter some of the problems reported in previous work on the modeling of starburst galaxies. Kewley et al. (2001) finds in the study of optical emission lines of starbursts that the FUV-field produced by *Starburst 99 v4.0* is too hard to be able to reproduce the observed line ratios (the number of photons in the 300 – 1000 Å range is too low compared to the highest energy photons between 100 – 300 Å). As a possible solution the implementation of line-blanketing in the atmospheres of high-mass stars was suggested, which is indeed incorporated in the current version of *Starburst 99 (v5.1)*. Nonetheless, the results of a more recent study of mid-infrared observations of starburst galaxies show similar problems (Rigby & Rieke 2004). Although these authors use a version of *Starburst 99* with line-blanketing implemented, the observed mid-infrared line ratios combined

with  $\text{He I}_{1.70\mu\text{m}}/\text{Br}10$  can only be explained by models assuming an IMF with a relatively low upper mass cutoff (40 – 60  $M_{\odot}$ ). In our work presented here there is no need to assume an unusually low  $M_{up}$ . As discussed in Section 4 we expect the fact that our models include dust, while the Rigby & Rieke models do not, plus changes in the modeling of W-R stars in *Starburst 99* to be responsible for the differences between our work and theirs. Furthermore, there may be computational differences in the photoionization codes used; we use *Mappings* and Rigby used *Cloudy*.

In spite of the improvements, several inconsistencies remain. The average ionization parameter for Givon's H II regions derived from the  $[\text{SIV}]/[\text{SIII}]$  versus  $[\text{NeIII}]/[\text{NeII}]$  plot, is lower than values indicated by the diagram plotting  $[\text{SIV}]/[\text{ArIII}]$  versus  $[\text{SIII}]/[\text{NeII}]$  ( $4 \cdot 10^7 \text{ cm s}^{-1} \leq q \leq 1.6 \cdot 10^8 \text{ cm s}^{-1}$  for the first diagram and  $8 \cdot 10^7 \text{ cm s}^{-1} \leq q \leq 8 \cdot 10^8 \text{ cm s}^{-1}$  for the latter). This discrepancy may originate from varying relative elemental abundances and/or differences between the detailed shape of the stellar FUV spectra in the models and in reality. Examining the data points in the  $[\text{SIV}]/[\text{ArIII}]$  versus  $[\text{SIII}]/[\text{NeII}]$  diagram (Fig. 11) suggests that the values for  $[\text{SIV}]/[\text{ArIII}]$  predicted by the models are too low and the strength of argon lines in the models is too high relative to the sulphur emission lines. Difficulties in the modeling of sulphur have been reported before (Martín-Hernández et al. (2002); Verma et al. (2003)). However, in these studies on ISO observations of galactic H II regions and starburst galaxies the sulphur abundance was found to be low compared

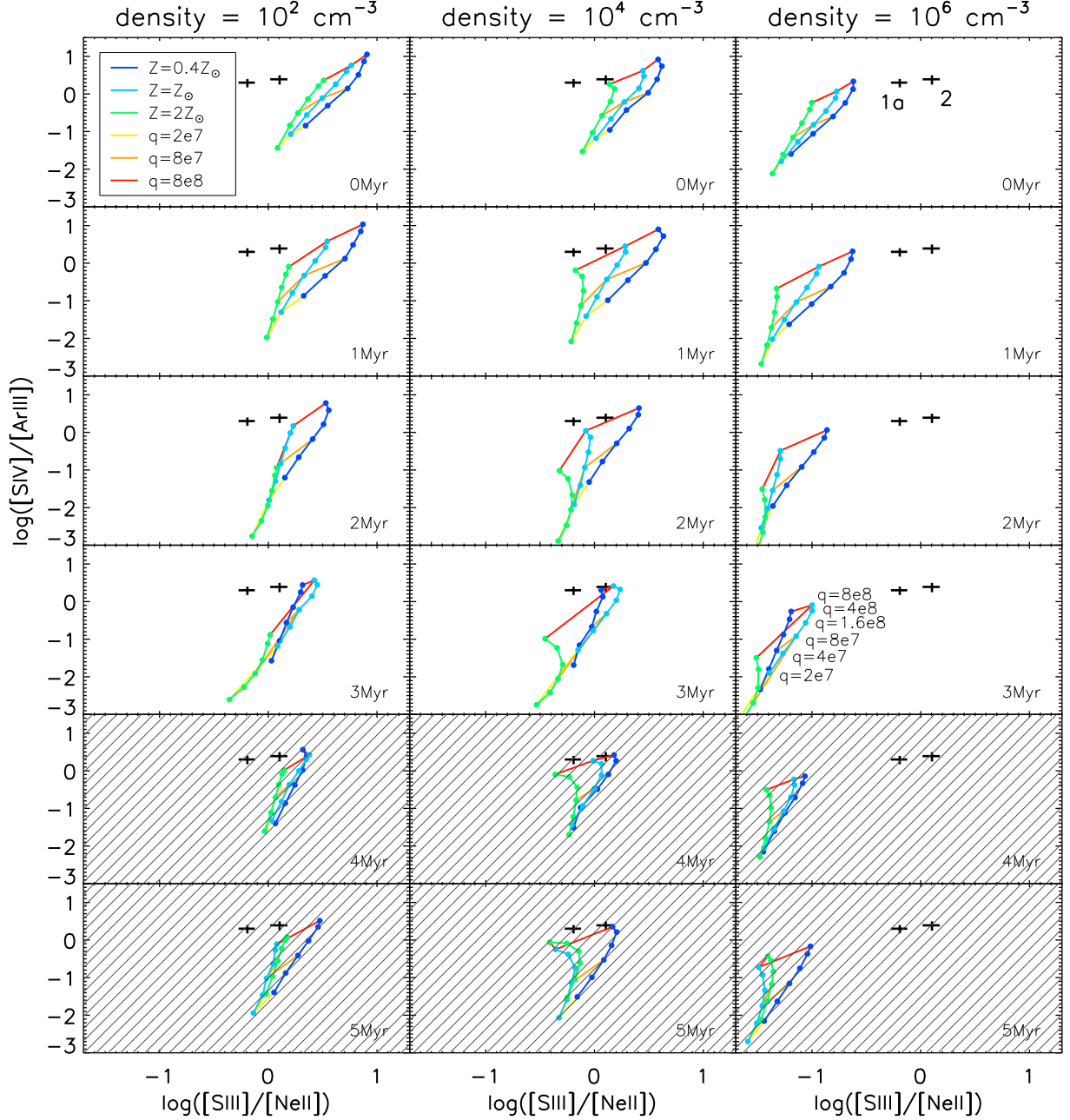


FIG. 15.— This plot is identical to Fig. 11 with the data points for the Antennae clusters included (crosses). The 4 Myr and 5 Myr panels are shaded, since we concluded from  $\text{EW}(\text{Br}\gamma)$  that the clusters are 3 Myr or younger (source 2; source 1a is  $\leq 2.5$  Myr). Error bars are given and the Antennae data points are extinction corrected as described in the text.

to neon and argon.

We modeled a very simple system, a single spherical stellar population, formed in an instantaneous burst of star formation wrapped in a thin shell of gas and dust. We assumed a Salpeter IMF between 0.1 and  $100 M_{\odot}$  for the stellar mass distribution of the clusters. Although the shape of the IMF is under constant debate, especially in extreme environments, such as in starbursts, Thornley et al. (2000) showed that differences in metallicity and ionization parameter have a much larger effect on mid-infrared line ratios than the shape of the

IMF. Given observational constraints, the assumption for the IMF upper mass cutoff is not expected to introduce a large error either. From the  $\text{EW}(\text{Br}\gamma)$  we know that both sources in the Antennae overlap region are 3 Myr or younger. Furthermore, Kunze et al. (1996) derived an effective temperature of 44,000 K from the  $[\text{Ne III}]/[\text{Ne II}]$  ratio, corresponding to the presence of a most massive star of  $60 M_{\odot}$  in the present day mass function (PDMF). The variation of several mid-infrared line ratios due to a different IMF upper mass cutoff during the first 3 Myr is shown to be a factor of two or

less (comparing  $M_{up}$  of  $50 M_{\odot}$  and  $100 M_{\odot}$  in Fig. 3 in Rigby & Rieke 2004). So the choice of upper mass cutoff in the range constrained by the observed age and effective temperature has a limited effect on the line ratios compared to varying density and ionization parameter.

The assumption of an instantaneous burst of star-formation does have a considerable impact on the mid-infrared emission lines. Because of the constant production of massive stars, the SED of a stellar population undergoing continuous star formation at a certain age is expected to be harder than that of a passively evolving stellar cluster formed in a single instantaneous burst of the same age. Thus under the assumption of constant star formation the ISM properties do not need to be as extreme (in density and ionization parameter) to reproduce the observed line ratios. Another source of major uncertainty is the modeling of stellar atmospheres. Since the mid-infrared emission line ratios are very sensitive to the detailed shape of the FUV spectra, the choice of atmospheric models have a large effect on the analysis of the observations. Furthermore, we know from local H II regions that the morphology of star-forming regions is usually very complex and nothing like a simple sphere. Since the regions discussed here are large, with a radius of 40-45 pc, we expect significant clumpy structure below our resolution limit. This issue will be addressed in the next Section. Lastly we mention the presence of shocks as another possible excitation mechanism. Indications for shocks being important in the Antennae overlap region are found from extraordinarily bright  $H_2$  emission (Haas et al. 2005). Part of the line emission could be shock excited, complicating the analysis.

### 8.2. Dense star-forming regions in the Antennae

Comparison of the model output with near- and mid-IR data of two clusters in the Antennae overlap region allow us to constrain the properties of the ISM surrounding the star clusters. Fitting  $[S\ IV]/[Ar\ III]$ ,  $[S\ III]/[Ne\ II]$ ,  $EW(Br\ \gamma)$  and  $He\ I_{1.70\ \mu m}/Br\ 10$  simultaneously results in a good fit of source 2 by a 3 Myr old stellar population with either solar or sub-solar metallicity, a density of  $10^4\ cm^{-3}$  and an ionization parameter of  $8 \cdot 10^8\ cm\ s^{-1}$ . Given that the metallicity of most star-forming regions in the overlap region was found to be around solar from optical observations (Bastian et al. 2006), we prefer the solution with solar metallicity.

It is evident from Fig. 15 that, unlike source 2, source 1a cannot be explained by a single component from the presented model grid. One possible solution to reproduce the observed line ratios is to extend the metallicity curves to higher values for the ionization parameter. Under the assumption that the metallicity of source 1a is around solar as well, the 2 Myr  $Z_{\odot}$  curve for a density of  $10^4\ cm^{-3}$  looks most promising. To estimate by how much  $q$  must be increased we extended this curve by adding the data points for a value for  $q$  of  $2 \cdot 10^9$  and  $4 \cdot 10^9\ cm\ s^{-1}$ . Figure 16 shows that the  $[S\ IV]/[Ar\ III]$  ratio saturates for such high ionization parameter values. The line ratios observed for source 1a can be fitted by a slightly super-solar metallicity, 2 Myr stellar population, embedded in matter with a density of  $10^4\ cm^{-3}$  that can be characterized by an ionization parameter of  $4 \cdot 10^9\ cm\ s^{-1}$ . Compared to previous estimates for  $q$  this is a very high value (see Fig.10 in Rigby & Rieke 2004, for ionization

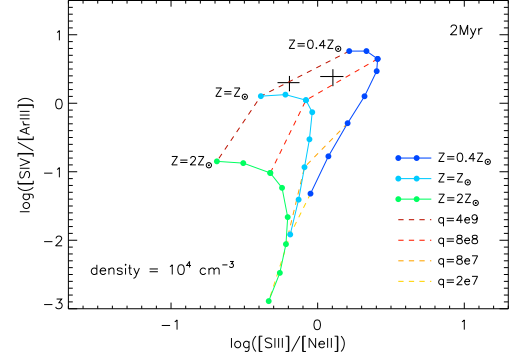


FIG. 16.— A blow-up of one individual panel of Fig. 15. The metallicity curves have been extended to higher values for the ionization parameter  $q$ . The solid curves correspond to different metallicities, black to  $Z = 0.4Z_{\odot}$ , dark grey to  $Z = Z_{\odot}$ , and light grey to  $Z = 2Z_{\odot}$  (a color figures can be found in the electronic edition). The dots corresponds to  $q = 2 \cdot 10^9, 4 \cdot 10^9, 8 \cdot 10^9, 1.6 \cdot 10^{10}, 4 \cdot 10^{10}, 8 \cdot 10^{10}, 2 \cdot 10^{11}$  and  $4 \cdot 10^{11}\ cm\ s^{-1}$ . The grey dashed lines connect curves of equal  $q$ .

parameters for a collection of local starbursts. The mean value for  $\log U$  is -2.3). However, since the star-forming regions in the Antennae are known to be very massive ( $\sim$  one million solar masses) and bright (Mengel et al. 2001), there is no reason to rule out this option before further analysis. A measurement of the  $[Ne\ III]$  line flux would help to obtain more robust constraints on  $q$  from our observations. Unfortunately it is impossible to obtain such observations with the same spatial resolution as our ground-based data. We note that a less extreme ionization parameter might be achieved by the use of the ultra-compact H II region models by Dopita et al. (2006a). This possibility will be explored in future work.

Since it is known from observations that star-forming regions are usually made up of a clumpy, structured, multi-phase ISM, we consider a second option to reproduce the mid-infrared characteristics of source 1a. We assumed a two-component medium by making linear combinations of model output spectra ( $f_1 \times \text{spectrum}_1 + f_2 \times \text{spectrum}_2$ , with  $f_1$  and  $f_2$  varying from 0.1 to 0.9 in steps of 0.1 and  $f_1 + f_2 = 1$ ; we only consider combinations with identical metallicity). In this way one can obviously create a large set of possible fits to the  $[S\ IV]/[Ar\ III]$  and  $[S\ III]/[Ne\ II]$  values of source 1a. It is interesting though that, without exception, all these possibilities require a high density. At least 70% of the matter from which these mid-infrared lines originate must have an average density of  $\geq 10^5\ cm^{-3}$ . If we fit our model results to the mid- and near-infrared lines simultaneously there is only one possible combination that can explain the data of source 1a that meets the assumption of solar metallicity: 90% of the radiating ISM can be characterized by a 0 Myr stellar population with a density of  $10^5\ cm^{-3}$  and an ionization parameter of  $8 \cdot 10^8\ cm\ s^{-1}$  and the remaining 10% by a 1 Myr solar metallicity population with a  $10^4\ cm^{-3}$  and an ionization parameter of  $8 \cdot 10^8\ cm\ s^{-1}$ . In reality a two component medium is an oversimplification as a model of an inhomogeneous star-forming region, but these results still provide a good estimate of the range of average properties we expect for these regions.

Altogether combining the data and the models indicates that source 1a is a very young stellar population

packed in a giant cloud of very dense gas and dust. During the first million years after the birth of the stellar population, one might expect the cluster still to be deeply buried in its natal cloud, reddened by far more obscuring matter than the  $A_V$  of 4.2 derived from near-IR data. The extinction is known to be patchy in this region, varying orders of magnitudes on scales comparable to our spatial resolution limit. Mid-IR narrow-band images revealed an object close to source 1a suffering much more extinction (Snijders et al. 2006). Since this object does not even have a counterpart detected in the near-IR, we concluded that the  $A_V$  must be in the order of 70 or larger. However, even if the extinction on source 1a is much larger than the  $A_V$  of 4.2 corrected for here, our results would not change, since the  $[S\text{IV}]/[Ar\text{III}]$  and  $[S\text{III}]/[Ne\text{II}]$  diagram is relatively insensitive to reddening (see the vector corresponding to  $A_V = 100$  in Fig. 11).

### 8.3. Evidence for a dense, clumpy ISM

Comparing the average density found in this work with ISM densities in the Antennae overlap region from the literature, we find that our value is comparable to the density of molecular gas derived from sub-mm  $^{12}\text{CO}$  and  $^{13}\text{CO}$  observations (Zhu et al. 2003). These observations indicate a two phase molecular gas medium, one component having a density  $n_{H_2}$  of  $1-8 \cdot 10^3 \text{ cm}^{-3}$  and a second denser component with  $n_{H_2} > 3 \cdot 10^4 \text{ cm}^{-3}$ , both average values for the whole overlap region.  $[Fe\text{III}]$  emission lines in near-infrared spectra with comparable spatial resolution as our data, indicate a somewhat lower ionized gas density than the value we found,  $10^{3.5} - 10^4 \text{ cm}^{-3}$  for source 1a (under the assumption that  $n_H \approx n_e$ . Source 2 is not addressed in this paper, Gilbert et al. 2000). In the same work a molecular gas density of  $10^5 \text{ cm}^{-3}$  is found from the analysis of  $H_2$  line emission.

Similar densities are locally observed only on very small scales in UCH II regions. Typically these star-forming clouds have a molecular gas density  $\geq 10^5 \text{ cm}^{-3}$  within a radius  $\leq 0.5 \text{ pc}$  (Churchwell 2002). With comparable average gas densities, but radii almost two orders of magnitude larger (the radius of source 1a and 2 is approximately 45 pc and 40 pc respectively Snijders et al. 2006), the star-forming regions in the Antennae bear more resemblance to extreme star-forming regions in ultra luminous infrared galaxies (ULIGs). A large fraction of the molecular gas in these sources is found to have densities larger than  $10^4 \text{ cm}^{-3}$  (Solomon et al. 1992). In a large sample of ULIGs Solomon et al. (1997) find somewhat lower molecular gas densities of  $10^3 - 10^4 \text{ cm}^{-3}$  for regions of 100 – 500 pc radius. In a subsequent paper, similar densities ( $2 \cdot 10^3 - 2 \cdot 10^4 \text{ cm}^{-3}$ ) are found for starburst regions in Arp193, Mrk273 and Arp220 for regions with 68 – 150 pc radii. Gas masses for these regions vary from 0.6 to  $1.1 \cdot 10^9 M_\odot$  (Downes & Solomon 1998).

If we assume a homogeneous distribution of the gas in spherical clouds the gas mass for source 1a is  $\sim 1.2 \cdot 10^8 M_\odot$  (gas density  $n_H$  of  $10^4 \text{ cm}^{-3}$ , taking the presence of helium into account, and a radius of 45 pc) and  $\sim 8.6 \cdot 10^7 M_\odot$  for source 2 (gas density  $n_H$  of  $10^4 \text{ cm}^{-3}$  and a radius of 40 pc). However, the assumption of a homogeneous medium is inconsistent with reality, as shown by the following argument. If we combine the results for the ionization parameter and the density derived from our

models with the Lyman continuum emission calculated from the extinction corrected  $Br\gamma$  flux (Table 2), we can get an estimate for the source size using Eq. 1. Under the assumption of case B recombination  $Q_{\text{Lyc}}$  is approximately  $9.3 \pm 0.9 \cdot 10^{52} \text{ s}^{-1}$  and  $6.7 \pm 0.7 \cdot 10^{52} \text{ s}^{-1}$  for source 1a and 2 respectively (this is in good agreement with determinations of  $Q_{\text{Lyc}}$  for source 1a by Gilbert et al. 2000, from near-infrared emission hydrogen lines and Hummel & Van der Hulst 1986, from thermal radio continuum flux, both find  $1 \cdot 10^{53} \text{ s}^{-1}$ ). If we focus on source 1a, and evaluate Eq. 1 with the appropriate value for  $Q_{\text{Lyc}}$ , a density  $n_H$  of  $10^4 \text{ cm}^{-3}$  and a value for  $q$  of  $4 \cdot 10^9 \text{ cm s}^{-1}$ , the radius of the emitting source should be  $\sim 4.4$  parsec (using the values for the two-component fit,  $n_H = 10^5 \text{ cm}^{-3}$  and  $q = 8 \cdot 10^8 \text{ cm s}^{-1}$ , results in a radius of 3.1 pc). This value is an order of magnitude smaller than the source radius measured from mid-infrared images, namely a half-light radius of 45 parsec.

This discrepancy implies the need for a more realistic, physical model than a single stellar population surrounded by a single-phase gas cloud. We adopt the geometry of a collection of  $N$  distinct H II regions (star-forming clumps) embedded in a giant molecular cloud, very similar to the proposed configuration in Fig. 7 of Förster Schreiber et al. (2001) for the nearby starburst M82. Observational support for this model can be found in mid-infrared images of source 1a. Although most of the clumpy substructure would be indistinguishable because of the spatial resolution of our observations, the general idea agrees with the finding of multiple ionizing sources embedded in an envelope of continuum and PAH emission (Snijders et al. 2006). Star clusters in cluster complexes are known to form following a certain mass distribution (Fall 2006; Dopita et al. 2006b, and references therein), so ideally one should perform Monte Carlo simulations of various different stellar populations buried in a clumpy ISM. However, for simplicity we assume  $N$  identical stellar populations. The Lyman continuum originating from each of these individual clusters is  $Q_{\text{Lyc}}/N$ . Combining the equation for the ionization parameter  $q$  for each individual region with the ionization balance for a Strömgren sphere (Eqs. 2 and 3), results in an indication of the size and number of individual H II regions.

$$q = \frac{Q_{\text{Lyc}}}{4\pi R^2 n_{\text{ion}}} \quad (2)$$

$$\frac{Q_{\text{Lyc}}}{N} = \frac{4}{3}\pi R_S^3 n_{\text{ion}}^2 \alpha_B \quad (3)$$

$\alpha_B$  is the recombination rate coefficient,  $2.6 \cdot 10^{-13} \text{ cm}^3 \text{ s}^{-1}$  at  $T_{\text{eff}} = 10,000 \text{ K}$ .  $R$  is the distance between the radiating source to the inner cloud boundary and  $R_S$  is the Strömgren radius. For typical H II regions most H II radiation originates from an ionized shell of gas around the Strömgren radius, so  $R \approx R_S$ . Solving this set of equations with identical values as used above results in a typical radius of 1.35 parsec and a number  $N$  of  $\sim 9$  clumps for source 1a. The Lyman continuum implies that within each of these clumps several hundreds of O-type stars are present ( $Q_{\text{Lyc}} = 9.6 \cdot 10^{51} \text{ s}^{-1}$  corresponds to the ionizing flux from  $\sim 225$  O3 stars, using the calibration of O stars from Martins et al. 2005). The total

ionized gas mass from all clumps added up is  $2.8 \cdot 10^5 M_{\odot}$ , approximately 3.5 orders of magnitude less than under the assumption of a homogeneous cloud of gas.

A nearby example of a system comparable to the model proposed here, a giant star-forming complex encompassing a handful of bright H II regions, can be found in M82 (at 3.6 Mpc distance, see Fig. 1 in Smith et al. 2006). Region A, an elongated cluster complex of  $\sim 50 - 100$  pc, shows rich substructure with several tens of star-forming clumps. The characteristics of one of these massive stellar clusters, M82-A1, is very similar to the properties inferred above for the star-forming clumps: the compact H II region has a radius of  $4.5 \pm 0.5$  pc and a density  $n_e$  of  $1800 \text{ cm}^{-3}$ . The central stellar population has an estimated age of 6.4 Myr and the total stellar mass is around a million solar masses. At the distance of the Antennae most information on the rich structure observed in M82's cluster complex A would be lost due to spatial resolution effects. It is very plausible that at a younger age the cluster complex would look very similar to one of the bright SSCs in the Antennae overlap region.

Further constraints on the stellar content of the star-forming clumps in our model can be determined by estimating the total stellar mass for source 1a by comparing the extinction corrected Br $\gamma$  flux with the *Starburst 99* output for a Salpeter IMF between 0.1 and  $100 M_{\odot}$ . Depending on age, which we constrained to be 0 – 2.5 Myr for source 1a, the total stellar mass is between  $3.2 \pm 0.3 \cdot 10^6 M_{\odot}$  (0 Myr) and  $4.2 \pm 0.4 \cdot 10^6 M_{\odot}$  (2.5 Myr; at the lower distance as found by Saviane et al. (2004) the mass would be lower by a factor of  $\sim 2.5$ ). This is in good agreement with the value of 3 million solar masses found by Mengel et al. (2001), but considerably lower than the  $16 \cdot 10^6 M_{\odot}$  by Gilbert et al. (2000). Note however that the studies of Gilbert and Mengel both use a lower mass cutoff of  $1 M_{\odot}$ , and Gilbert adopts an age of 4 Myr. With a total stellar mass of 3 – 4 million solar masses, each individual star-forming clump would host  $3 - 4 \cdot 10^5 M_{\odot}$  of stars, resulting in a stellar density of  $3 - 4 \cdot 10^4 M_{\odot} \text{ pc}^{-3}$ , which is equivalent to a density  $n_H$  of  $0.9 - 1.2 \cdot 10^6 \text{ cm}^{-3}$ . This implies very high star-formation efficiencies if we assume these stellar populations to be formed from typical dense molecular clouds (cloud core densities  $n_H \approx 10^6 - 10^7 \text{ cm}^{-3}$ ). Studies of the most massive galactic star-forming regions and of super star clusters (SSC) in various starburst galaxies found comparable equivalent densities, as summarized in Fig. 1 by Tan (2006). In this Figure source 1a would end up between the Arches cluster in the Milky Way and the central SSC in NGC5253.

Although our findings for the average stellar mass densities are similar to results for other massive star-forming regions, there are scenarios that require less extreme mass densities. For a stellar mass distribution with relatively little low-mass stars compared to 'Salpeter' (e.g. a Miller-Scalo, Kroupa, Chabrier, or top-heavy IMF), the mass within the 1.35 pc radius would be less. Indications for the existence of an IMF dominated by massive stars is found in several massive star-forming regions, in the center of our galaxy (Nayakshin & Sunyaev 2005) as well as in other starburst galaxies (Doane & Mathews 1993; Rieke et al. 1993). Such a deviant IMF could be the result of stellar winds and supernova explosions of the high-

mass stars shutting off the slower formation process of low-mass stars by expelling the available matter from the star-forming region. Another option is mass segregation within the stellar cluster. The high-mass stars in clusters are often observed to be more centrally concentrated than the low-mass stars. This is possibly caused by rapid inward migration of massive stars (Freitag et al 2006; Portegies Zwart et al 1999). The mid-infrared emission lines we observe, originate predominantly from the highest mass stars, and the cluster core, where most of these massive stars reside after mass segregation, would be deficit in low-mass stars. This mechanism would not affect the total cluster mass, but would lower the derived density in the cluster core.

Another plausible model for the morphology of a cluster complex would be several star-forming clumps embedded in a large cloud of diffuse, ionized gas. However, from our mid-infrared data we do not see evidence for a significant fraction of low density ionized gas. Gas with a density of  $10^2 \text{ cm}^{-3}$  would boost the fluxes of the emission lines with the lowest critical densities (e.g. [S III] at  $33.48 \mu\text{m}$ ). Consequently, the presence of a large amount of low density ionized gas would leave its fingerprints on the observed line ratios, which would have been recovered as possible solutions in the two-component medium fits. The only possibility would be a component of low density gas characterized by a very high ionization parameter ( $q \geq 5 - 10 \cdot 10^9 \text{ cm s}^{-1}$ ). As we have seen in Fig. 16 the [S IV]/[Ar III] ratio saturates at high values of  $q$ , causing a bend in the metallicity curves towards lower [S III]/[Ne II] values. In this way it would be possible to have a significant contribution from low density gas to the observed line ratios. We consider this option highly unlikely though. A combination of low density and such high ionization parameter would not arise, since  $q$  is inversely proportional to  $R^2$  and we expect the diffuse gas to be at a relatively high distance from the ionizing sources on average, which would suppress  $q$  (Eq. 1). Furthermore, the typical ionization parameters for star-forming regions in starburst galaxies derived from observations are lower (Fig. 10 in Rigby & Rieke 2004), as well as the values for  $q$  predicted by models (Dopita et al. 2006a).

## 9. CONCLUSIONS

The recent advent of the first generation of mature mid-infrared instruments on ground-based telescopes was one of the main motivations for this work. With mid-infrared observations being performed routinely on various 8-meter class telescopes nowadays, rich new data sets rapidly become available. A lot of work has been done based on space-based mid-infrared observations over the last decades. Because of the characteristics of the earth's atmosphere, ground-based work is limited to the spectral features observable from the atmospheric windows of reasonably good transmission. So, in this work we focus on the features that are available from ground-based observations.

We have used the stellar population synthesis model *Starburst 99* combined with the photoionization code *Mappings* to simulate mid-infrared emission lines of star-forming regions in starburst galaxies. We have shown that the models succeed in reproducing the observed line ratios of H II and starburst regions with a wide variety of

properties, ranging from diffuse to very dense systems.

Applying the model results in an analysis of the mid-infrared data of SSCs in the Antennae overlap region, leads to the conclusion that the average ionized gas density in these star-forming region is very high. Source 2, the mid-infrared counterpart of a blue cluster complex, can best be modeled by a 3 Myr old stellar population embedded in dense matter,  $n_H = 10^4 \text{ cm}^{-3}$ , that can be characterized by an ionization parameter of  $8 \cdot 10^8 \text{ cm s}^{-1}$ . The observed line ratios for source 1a, corresponding to the highly reddened cluster WS95-80 in Whitmore & Schweizer (1995), can only be reproduced by assuming an extremely high ionization parameter  $q = 4 \cdot 10^9 \text{ cm s}^{-1}$  in combination with a 2 Myr stellar population and  $10^4 \text{ cm}^{-3}$  density. We also considered a two-phase ISM by fitting linear combinations of model output. This resulted in a younger stellar population of 0 – 1 Myr, surrounded by  $10^5 \text{ cm}^{-3}$  gas characterized by  $q = 8 \cdot 10^8 \text{ cm s}^{-1}$ .

Detailed comparison of the mid-infrared emission lines with the images shows us that the ISM in these two star-

forming regions is as expected far from homogeneous. As a possible geometrical model we propose several individual star-forming clumps embedded in a giant molecular cloud. This model is supported by the morphology of the source in the mid-infrared images, showing two ionizing sources within a large enveloping cloud of continuum and dust emission. The typical number of H II regions within the molecular cloud of  $\sim 40 \text{ pc}$  radius is 9, each with a radius in the order of 1.35 pc (source 1a). Such morphology is observed in nearby starbursts as well. Each of these clumps would contain  $\sim 225 \text{ O3 stars}$  and have a gas density of  $320 \text{ M}_\odot/\text{pc}^3$  ( $n_H = 10^4 \text{ cm}^{-3}$ ).

We thank the Paranal Observatory Team for their support. Furthermore, we thank Brent Groves for advice and fruitful discussions that improved the paper. Part of this work was funded by the Leids Kerkhoven-Bosscha Fonds, we thank them for their support.

## REFERENCES

- Bastian, N., Emsellem, E., Kissler-Patig, M. & Maraston, C., 2006, *A&A*, 445, 471
- Benjamin, R. A., Skillman, E. D. & Smits, D. P., 1999, *ApJ*, 514, 307
- Blain, A. W., Smail, I., Ivison, R. J. & Kneib, J.-P. 1999, *MNRAS* 302, 632
- Brandl, B. R. et al, 2005, *ApJ*, 635, 280
- Cohen, M., Walker, R. G., Carter, B., Hammersley, P., Kidger, M. & Noguchi, K., 1999, *AJ* 117, 1864
- Churchwell, E., 2002, *ARA&A*, 40, 27
- Dale D. A. et al, 2006, *ApJ*, 646, 161
- Doane, J. S & Mathews, W. G., 1993, *ApJ*, 419, 573
- Dopita, M. A., Kewley, L. J., Heisler, C. A. & Sutherland, R. S., 2000, *ApJ*, 542, 224
- Dopita, M. A., Groves, B. A., Sutherland, R. S., Binette, L. & Cecil, G., 2002, *ApJ*, 572, 753
- Dopita, M. A. et al., 2005, *ApJ*, 619, 755
- Dopita, M. A. et al., 2006, *ApJ*, 647, 244
- Dopita, M. A. et al., 2006, *ApJ* 639, 788
- Downes, D. & Solomon, P. M., 1998, *ApJ*, 507, 615
- Draine, B. T., 1989, in *ESLAB Symp. 22, IR Spectroscopy in Astronomy*, ed. B. H. Kaldeich, ESA SP-290, 93
- Draine, B. T., 2003, *ARA&A*, 41, 241
- Fall, M. S., 2006, *ApJ*, 652, 1129
- Ferland, G. J., 2001, *Hazy, A Brief Introduction to CLOUDY* 94.00
- Förster Schreiber, N. M., Genzel, R., Lutz, D., Kunze, D. & Sternberg, A. 2001, *ApJ*, 552, 544
- Freitag, M., Gürkan, M. A. & Rasio, F. A., 2006, *MNRAS*, 368, 141
- Gilbert, A. M. et al, 2000, *ApJ*, 533, 57
- Giveon, U, Sternberg, A., Lutz, D., Feuchtgruber, H. & Pauldrach, A. W. A., 2002, *ApJ*, 566, 880
- Groves, B. A., Dopita, M. A. & Sutherland, R. S., 2004, *ApJS*, 153, 9
- Haas, M., Chini, R. & Klaas, U., 2005, *A&A*, 433, 17
- Heckman, T. M., 1998, in *ASP Conf. Ser. 148, Origins*, ed. C. E. Woodward, J. M. Shull, & H. A. Thronson, Jr. (San Francisco: ASP), 127
- Hillier, D. J. & Miller, D. L., 1998, *ApJ*, 496, 407
- Hummel, E. & Van der Hulst, J. M. 1986, *A&A*, 155, 151
- Hummer, D. G. & Storey, P. J., 1987, *MNRAS*, 224, 801
- Jones, A. P., Tielens, A. G. G. M. & Hollenbach, D. J., 1996, *ApJ*, 469, 740
- Kennicutt, R. C. et al, 2003, *PASP*, 115, 928
- Kewley, L. J., Dopita, M. A.; Sutherland, R. S., Heisler, C. A. & Trevena, J., 2001, *ApJ*, 556, 121
- Kroupa, P., 2007, in *ASP Conf. Ser., Resolved Stellar Populations*, ed. Valls-Gabaud, D. & Chavez, M. (San Francisco: ASP), in press (astro-ph/0703124)
- Kunze, D. et al, 1996, *A&A*, 315, 101
- Kurucz, R., 1992, in *IAU Symp. 149, The Stellar Populations of Galaxies*, ed. Barbuy, B. & Renzini, A. (Dordrecht:Kluwer), 225
- Lagage, P. O. et al, 2004, *The Messenger* 117, 12
- Leitherer C. et al., 1999, *ApJS*, 123, 3
- Leitherer C. & Heckman, T. M., 1995, *ApJS*, 96, 9
- Lejeune, Th., Cuisinier, F. & Buser, F., 1997, *A&AS*, 125, 229
- Lumsden S. L., Puxley P. J. & Hoare M. G., 2001, *MNRAS*, 320, 83
- Maeder, A. & Meynet, G., 1994, *A&A*, 287, 803
- Martín-Hernández, N. L. et al., 2002, *A&A*, 381, 606
- Martín-Hernández, N. L., Schaerer, D. & Sauvage, M., 2005, *A&A*, 429, 449
- Martins F., Schaerer, D. & Hillier, D. J., 2005, *A&A*, 436, 1049
- Mengel, S., Lehnert, M. D., Thatte, N., Tacconi-Garman, L. E. & Genzel, R., 2001, *ApJ*, 550, 280
- Mengel, S., Lehnert, M. D., Thatte, N. & Genzel, R., 2005, *A&A*, 443, 41
- Mirabel, I. F. et al. 1998, *A&A* 333, L1
- Moorwood A. et al, 1998, *The Messenger*, 94, 7
- Nayakshin S. & Sunyaev R., 2005, *MNRAS*, 364, 23
- Pauldrach, A. W. A., Hoffmann, T. L. & Lennon M., 2001, *A&A*, 375, 161
- Portegies Zwart S. F., Makino J., McMillan S. L. W. & Hut P., 1999, *A&A*, 348, 117
- Rieke, G. H., Loken, K., Rieke, M. J. & Tamblyn, P., 1993, *ApJ*, 412, 99
- Rigby, J. R. & Rieke, G. H., 2004, *ApJ*, 606, 237
- Savage B. D. & Sembach K. R., 1996, *ApJ*, 470, 893
- Saviane, I., Hibbard, J. E. & Rich, M. R., 2004, *AJ* 127, 660
- Smail, I., Ivison, R. J., Blain, A. W. & Kneib, J.-P. 2002, *MNRAS* 331, 495
- Smith, L. J., Norris, R. P. F. & Crowther, P. A., 2002, *MNRAS* 337, 1309
- Smith, L. J., Westmoquette, M. S., Gallagher, J. S., O’Connell, R. W., Rosario, D. J. & de Grijs, R., 2006, *MNRAS*, 370, 513
- Snijders, L., Van der Werf, P. P., Brandl, B. R., Mengel, S., Schaerer, D., Wang, Z., 2006, *ApJ*, 648, 25
- Solomon, P. M., Downes, D. & Radford, S. J. E., 1992, *ApJ*, 387, 55
- Solomon, P. M., Downes, D., Radford, S. J. E. & Barrett J. W., 1997, *ApJ*, 478, 144
- Tan, J. C., 2006, in *IAU Symp. 237, Triggered Star Formation in a Turbulent ISM*, ed. B. G. Elmegreen & J. Palous, 256

- Thornley, M. D., Förster-Schreiber, N. M., Lutz, D., Genzel, R., Spoon, H. W. W.; Kunze, D. & Sternberg, A., 2000, *ApJ*, 539, 641
- Tielens, A. G. G. M., 2005, "The Physics and Chemistry of the Interstellar Medium", Cambridge University Press
- Vázquez, G. A. & Leitherer C., 2005, *ApJ* 621, 695
- Verma, A., Lutz, D., Sturm, E., Sternberg, A., Genzel, R. & Vacca, W., 2003 *A&A*, 403, 829
- Whitmore, B. W. & Schweizer, F., 1995, *AJ*, 109, 960
- Whitmore, B. W. et al, 2005, *AJ*, 130,2104
- Zhu, M., Seaquist, E. R. & Kuno, N., 2003, *ApJ*, 588, 243